Publication Year	2020
Acceptance in OA	2025-02-20T09:55:06Z
Title	ARES. II. Characterizing the Hot Jupiters WASP-127 b, WASP-79 b, and WASP-62b with the Hubble Space Telescope
Authors	GUILLUY, Gloria
Publisher's version (DOI)	10.3847/1538-3881/ab94a3
Handle	http://hdl.handle.net/20.500.12386/36085
Journal	THE ASTRONOMICAL JOURNAL
Volume	160

The Astronomical Journal, 160:109 (17pp), 2020 September https://doi.org/10.3847/1538-3881/ab94a3
© 2020. The American Astronomical Society. All rights reserved.

ARES. II. Characterizing the Hot Jupiters WASP-127 b, WASP-79 b, and WASP-62b with the Hubble Space Telescope*

Nour Skaf[1,2], Michelle Fabienne Bieger[3], Billy Edwards[2], Quentin Changeat[2], Mario Morvan[2], Flavien Kiefer[4], Doriann Blain[1], Tiziano Zingales[5], Mathilde Poveda[6,7], Ahmed Al-Refaie[2], Robin Baeyens[8], Amélie Gressier[1,4,9], Gloria Guilluy[10,11], Adam Yassin Jaziri[5], Darius Modirrousta-Galian[12,13], Lorenzo V. Mugnai[14], William Pluriel[5], Niall Whiteford[15,16], Sam Wright[2], Kai Hou Yip[2], Benjamin Charnay[1], Jérémy Leconte[5], Pierre Drossart[1], Angelos Tsiaras[2], Olivia Venot[6], Ingo Waldmann[2], and Jean-Philippe Beaulieu[4,17]

[1] LESIA, Observatoire de Paris, Universitè PSL, CNRS, Sorbonne Université, Université de Paris, 5 place Jules Janssen, F-92195 Meudon, France
nour.skaf@obspm.fr
[2] Department of Physics and Astronomy, University College London, London, UK
[3] College of Engineering, Mathematics and Physical Sciences, University of Exeter, North Park Road, Exeter, UK
[4] Sorbonne Universités, UPMC Université Paris 6 et CNRS, UMR 7095, Institut d'Astrophysique de Paris, 98 bis bd Arago, F-75014 Paris, France
[5] Laboratoire d'astrophysique de Bordeaux, Univ. Bordeaux, CNRS, B18N, allée Geoffroy Saint-Hilaire, F-33615 Pessac, France
[6] Laboratoire Interuniversitaire des Systèmes Atmosphériques (LISA), UMR CNRS 7583, Université Paris-Est-Créteil, Université de Paris, Institut Pierre Simon Laplace, Créteil, France
[7] Maison de la Simulation, CEA, CNRS, Univ. Paris-Sud, UVSQ, Université Paris-Saclay, F-91191 Gif-sur-Yvette, France
[8] Instituut voor Sterrenkunde, KU Leuven, Celestijnenlaan 200D bus 2401, B-3001 Leuven, Belgium
[9] LATMOS, CNRS, Sorbonne Université UVSQ, 11 boulevard d'Alembert, F-78280 Guyancourt, France
[10] Dipartimento di Fisica, Università degli Studi di Torino, via Pietro Giuria 1, I-10125 Torino, Italy
[11] INAF—Osservatorio Astrofisico di Torino, Via Osservatorio 20, I-10025 Pino Torinese, Italy
[12] INAF—Osservatorio Astronomico di Palermo, Piazza del Parlamento 1, I-90134 Palermo, Italy
[13] University of Palermo, Department of Physics and Chemistry, Via Archirafi 36, Palermo, Italy
[14] La Sapienza Universitá di Roma, Department of Physics, Piazzale Aldo Moro 2, I-00185 Roma, Italy
[15] Institute for Astronomy, University of Edinburgh, Blackford Hill, Edinburgh EH9 3HJ, UK
[16] Centre for Exoplanet Science, University of Edinburgh, Edinburgh EH9 3FD, UK
[17] School of Physical Sciences, University of Tasmania, Private Bag 37 Hobart, Tasmania 7001, Australia
Received 2019 December 1; revised 2020 May 11; accepted 2020 May 17; published 2020 August 12

Abstract

This paper presents the atmospheric characterization of three large, gaseous planets: WASP-127 b, WASP-79 b, and WASP-62 b. We analyzed spectroscopic data obtained with the G141 grism (1.088–1.68 μm) of the Wide Field Camera 3 on board the Hubble Space Telescope using the `Iraclis` pipeline and the TauREx3 retrieval code, both of which are publicly available. For WASP-127 b, which is the least dense planet discovered so far and is located in the short-period Neptune desert, our retrieval results found strong water absorption corresponding to an abundance of $\log(H_2O) = -2.71^{+0.78}_{-1.05}$ and absorption compatible with an iron hydride abundance of $\log(FeH) = -5.25^{+0.88}_{-1.10}$, with an extended cloudy atmosphere. We also detected water vapor in the atmospheres of WASP-79 b and WASP-62 b, with best-fit models indicating the presence of iron hydride, too. We used the Atmospheric Detectability Index as well as Bayesian log evidence to quantify the strength of the detection and compared our results to the hot Jupiter population study by Tsiaras et al. While all the planets studied here are suitable targets for characterization with upcoming facilities such as the James Webb Space Telescope and Ariel, WASP-127 b is of particular interest due to its low density, and a thorough atmospheric study would develop our understanding of planet formation and migration.

Unified Astronomy Thesaurus concepts: Exoplanet astronomy (486); Exoplanet atmospheres (487); Astronomy data analysis (1858); Hubble Space Telescope (761)

1. Introduction

The currently known exoplanet population displays a wide range of masses, radii, and orbits. Although many planets have been detected and it is thought that they are common in our Galaxy (Cassan et al. 2012; Wright et al. 2012; Batalha et al. 2013; Dressing & Charbonneau 2013; Howard 2013), our current knowledge of their atmospheric characteristics is still very limited. Examining the atmospheres of exoplanets further unveils their planetary properties, with their study made possible by various methods, including transit spectroscopy (e.g., Tinetti et al. 2007; Swain et al. 2008). Facilities such as the Hubble Space Telescope (HST) and the Spitzer Space Telescope, as well as some ground-based observatories, have provided constraints on these properties for a limited number of targets and, in some cases, have identified the key molecules present in their atmospheres while also detecting the presence of clouds and probing their thermal structure (e.g., Brogi et al. 2012; Majeau et al. 2012; Stevenson et al. 2014; Sing et al. 2016; Fu et al. 2017; Hoeijmakers et al. 2018; Tsiaras et al. 2018, 2019; Pinhas et al. 2019; Edwards et al. 2020a; Ehrenreich et al. 2020).

This paper presents the analysis of data from Hubble's public archive for the exoplanets WASP-127 b, WASP-79 b, and WASP-62 b. They are all inflated, with low eccentricities and short orbital periods around bright stars. Table 1 presents the stellar and planetary parameters for each of these targets.

WASP-127 b is an ideal target for spectroscopic studies, given its unusually low density (with a super-Jupiter radius and a sub-Saturn mass). It is located in the short-period Neptune desert, where it is expected that planets might not survive photoevaporation (Mazeh et al. 2016; Owen & Lai 2018). However,

* ARES: Ariel Retrieval of Exoplanets School.

Table 1
Target Parameters

Parameter	WASP-127 b	WASP-79 b	WASP-62 b
	Stellar Parameters		
Spectral type	G5	F5	F7
$T_{\rm eff}$ [K]	5750 ± 85	6600 ± 100	6230 ± 80
log g (cgs)	3.9	4.06 ± 0.15	4.45 ± 0.10
[Fe/H]	−0.18 ± 0.06	0.03	0.04
	Planetary Parameters		
P [days]	4.17807015 ± 2.10^{-6}	3.662387 ± 4.10^{-6}	4.411953 ± 4.10^{-6}
$T_{\rm mid}$ [BJD_{TDB}-2450000]	8138.670144	7815.89868	5855.39195
i [°]	$88.2^{+1.1}_{-0.9}$	86.1 ± 0.2	$88.5^{+0.4}_{-0.7}$
$M_{\rm P}[M_{\rm J}]$	0.18 ± 0.02	0.85 ± 0.8	0.58 ± 0.03
$R_{\rm P}[R_{\rm J}]$	1.37 ± 0.04	1.53 ± 0.04	$1.34^{+0.05}_{-0.03}$
$T_{\rm eq,A=0}$ [K]	1400 ± 24	$1716.2^{+25.8}_{-24.4}$	$1475.3^{+25.1}_{-10}$
$R_P/R_\star$	$0.09992^{+0.0028}_{-0.0029}$	$0.09609^{+0.0023}_{-0.0027}$	$0.1091^{+0.0038}_{-0.0023}$
$a/R_\star$	7.846	6.069	9.5253
References	Palle et al. (2017)	Brown et al. (2017)	Brown et al. (2017)

Table 2
HST/WFC3 Data Summary

Planet	Median Epoch (MJD)	Mean Exposure Time (s)	Number of Spectra	PI Name	Proposal ID
WASP-127 b	58217.51310	95.782	74	Jessica Spake	14619
WASP-79 b	57815.37216	138.381	64	David Sing	14767
WASP-62 b	57857.82823	138.381	61	David Sing	14767

photoevaporation is strongly case dependent, and this planet receives a relatively low extreme ultraviolet flux (Chen et al. 2018). Potential explanations for its inflation include tidal heating, enhanced atmospheric opacity, ohmic heating, and reinflation by the host star during inward migration (Batygin & Stevenson 2010; Leconte et al. 2010; Batygin et al. 2011; Rauscher & Menou 2013; Lithwick & Wu 2014). Both WASP-62 b and WASP-79 b are believed to have an evaporating atmosphere, with mass-loss rates estimated at $\approx$11 g s^{-1} (Bourrier et al. 2015). WASP-79 b, which has a polar orbit, was originally detected through an aberration in the radial velocity due to the Rossiter–McLaughlin effect (Addison et al. 2013).

All spectral data presented herein were acquired with the G141 grism (1.088–1.68 μm) of the HST/Wide Field Camera 3 (WFC3) camera, and details regarding each observation can be found in Table 1. In Section 2, we detail how the data were reduced with the `Iraclis` pipeline (Tsiaras et al. 2016b), following the approach described by Tsiaras et al. (2018) and summarized here. In Section 2.3, we describe the TauREx retrieval code used to analyze the reduced spectra (Waldmann et al. 2015a, 2015b; Al-Refaie et al. 2019), along with the initial parameters and priors used. Our results can be found in Section 3, followed by a discussion on our findings and the implications they hold for future missions, including simulations of data from Ariel and the James Webb Space Telescope (JWST).

2. Methodology

2.1. HST Observations

Data reduction and calibration were performed using `Iraclis`, software developed in Tsiaras et al. (2016b) and available on GitHub;[18] it has been used to extract HST spectra in multiple studies, including Tsiaras et al. (2016a, 2018, 2019). We used the Mikulski Archive for Space Telescopes[19] to assess the spectroscopic observational data of WASP-127 b, WASP-79 b, and WASP-62 b, and information about the observations can be found in Table 2. The WASP-127 b proposal was led by Jessica Spake while David Sing was the PI for the observations of WASP-79 b and WASP-62 b. Although more data are available from additional instruments, we have restricted our study to HST/WFC3 data, in order to maintain consistency in comparing the analysis of the planets.

2.2. Data Analysis

The planets in this paper were analyzed to be comparable to the 30 planets studied in Tsiaras et al. (2018). We followed the same methodology as summarized below; differences between our studies are stated explicitly.

Our analysis began with raw spatially scanned spectroscopic images, with data reduction and correction steps performed in the following order: zero-read subtraction, reference pixel correction, nonlinearity correction, dark current subtraction, gain conversion, sky-background subtraction, calibration, flat-field correction, and bad pixels and cosmic-ray correction.

Following the reduction process, the flux was extracted from the spatially scanned spectroscopic images to create the final transit light curves per wavelength band. We considered one broadband (white) light curve covering the whole wavelength range in which the G141 grism is sensitive (1.088–1.68 μm)

[18] https://github.com/ucl-exoplanets/Iraclis
[19] https://archive.stsci.edu/hst/

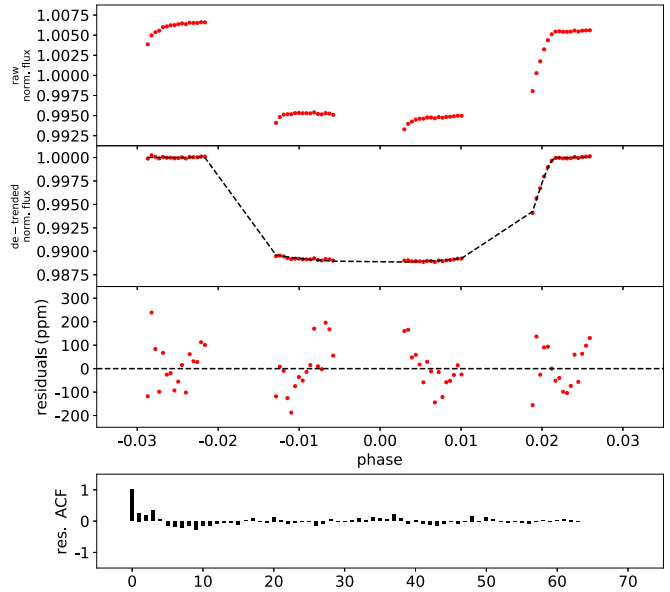

Figure 1. Results of the white-light curve of WASP-127 b. Top: raw light curve, after normalization. Second: light curve, divided by the best-fit model for the systematics. Third: residuals. Bottom: autocorrelation function of the residuals.

and spectral light curves with a resolving power of 70 at 1.4 μm. When extracting the spectral light curves, `Iraclis` accounts for the geometric distortions induced by the tilt of the detector in the WFC3 infrared channel. The bands of the spectral light curves are selected such that the signal-to-noise ratio is approximately uniform across the planetary spectrum. We extracted our final light curves from the differential, nondestructive reads. Prior to light-curve fitting, we chose to discard the first HST orbit of each visit, as these exhibit much stronger hooks than subsequent orbits.

Our white-light curves were fit using literature values, and the only free parameters, other than the coefficients for Hubble systematics, were the planet-to-star radius ratio and the transit midtime. This is motivated by the gaps in the observations, caused by Earth obscuration, which often means the ingress and egress of the transit are missed, limiting our ability to refine the semimajor axis to star radius ratio and the inclination of the planet's orbit. The limb-darkening coefficients were selected from the quadratic formula by Claret (2000), using the stellar parameters in Table 1. Figure 1 shows the raw white-light curve, the detrended white-light curve, and the fitting residuals for WASP-127 b while Figure 2 shows the fits of the spectral light curves for each wavelength bin. Similar plots for WASP-79 b and WASP-62 b are shown in Figures 3 and 4.

2.3. Atmospheric Characterization

The reduced spectra obtained using `Iraclis` were thereafter fitted using the publicly available[20] Bayesian atmospheric retrieval framework TauREx3 (Al-Refaie et al. 2019). TauREx uses the nested sampling code Multinest (Feroz et al. 2009) to explore the likelihood space of atmospheric parameters and features highly accurate line lists from the ExoMol project (Tennyson et al. 2016), along with those from HITRAN and HITEMP (Rothman et al. 1987, 2010). In our retrieval analysis, we used 750 live points and an evidence tolerance of 0.5.

[20] https://github.com/ucl-exoplanets/TauREx3_public

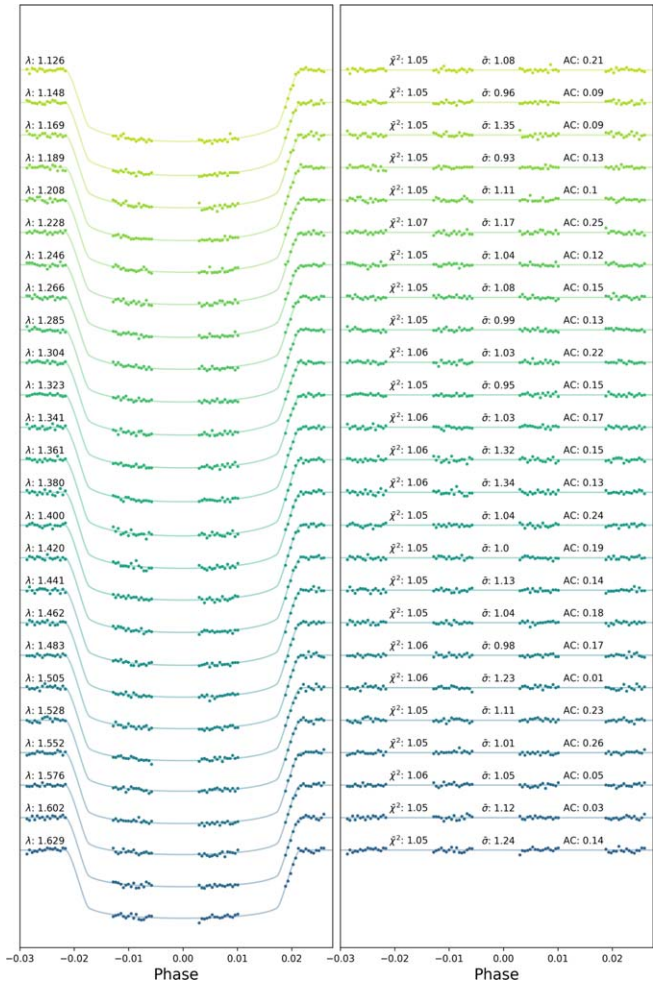

Figure 2. Spectral light curves fitted with `Iraclis` for the transmission spectra where, for clarity, an offset has been applied. Left: the detrended spectral light curves with best-fit model plotted. Right: residuals from the fitting with values for the Chi-squared (χ^2), the standard deviation of the residuals with respect to the photon noise ($\bar{\sigma}$), and the autocorrelation (AC). Similar plots for WASP-79 b and WASP-62 b are shown in Figures 3 and 4. The mean $\bar{\sigma}$ for each of the three planets is between 1.02 and 1.25 times the photon noise.

Several molecular opacities have been tested to model the spectra of the observations; in this publication, we considered five trace gases: H_2O (Polyansky et al. 2018), CH_4 (Yurchenko & Tennyson 2014), CO (Li et al. 2015), CO_2 (Rothman et al. 2010), NH_3 (Yurchenko et al. 2011), and FeH (Dulick et al. 2003). In the wavelength range covered by G141, water vapor is the dominant spectral feature, but these other molecules can present detectable signals, particularly FeH (Tennyson & Yurchenko 2018). Clouds are fitted assuming a gray opacity model.

2.3.1. General Setup

In this study we use the plane-parallel approximation to model the atmospheres, with pressures ranging from 10^{-2} to 10^6 Pa, uniformly sampled in log-space with 100 atmospheric layers. We included the Rayleigh scattering and the collision-induced absorption (CIA) of H_2–H_2 and H_2–He (Abel et al. 2011, 2012; Fletcher et al. 2018). A summary of the fitted retrieval parameters is given in Table 1. For consistency, the same parameter bounds have been applied for all three planets. Constant molecular abundance profiles were used and allowed

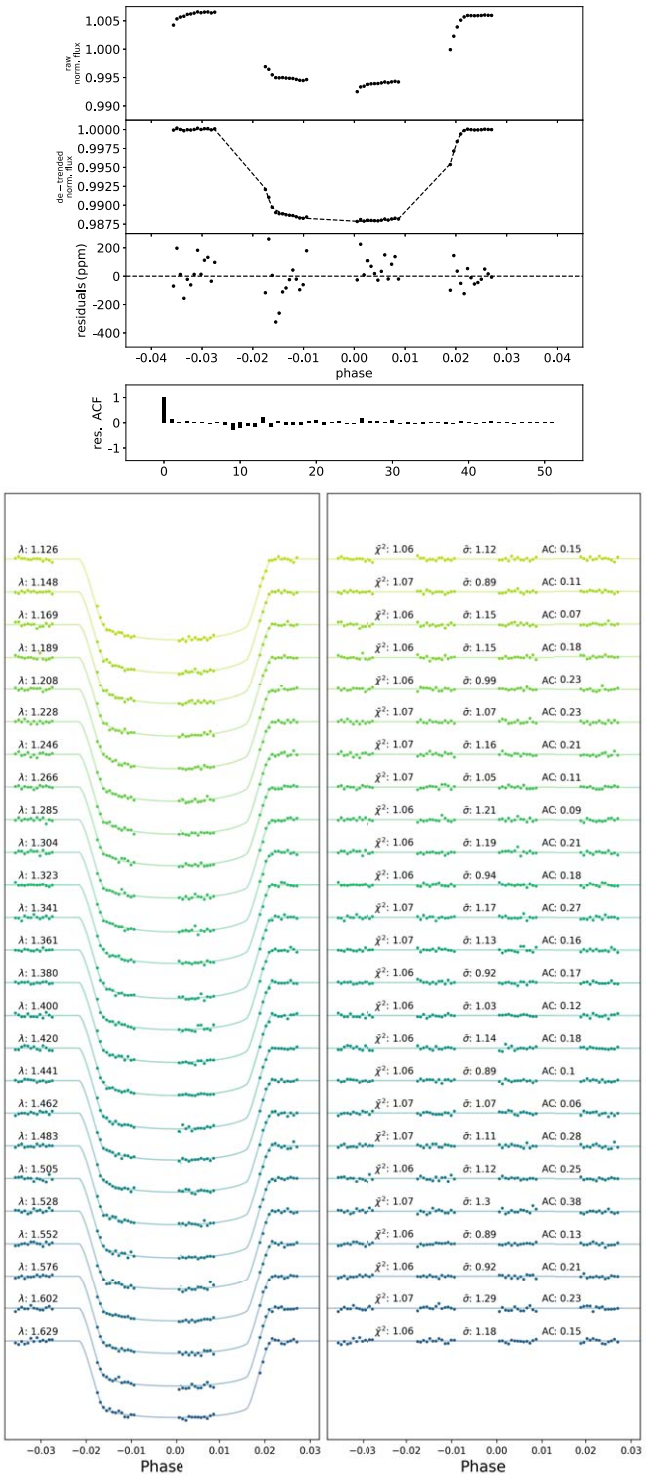

Figure 3. Top figure: results of the white-light curve of WASP-79 b. Top: raw light curve, after normalization. Second: light curve, divided by the best-fit model for the systematics. Third: residuals. Bottom: autocorrelation function of the residuals. Bottom figure: spectral light curves fitted with`Iraclis`for the transmission spectra where, for clarity, an offset has been applied. Left: the detrended spectral light curves with best-fit model plotted. Right: residuals from the fitting with values for the Chi-squared (χ^2), the standard deviation of the residuals with respect to the photon noise ($\bar{\sigma}$), and the autocorrelation (AC).

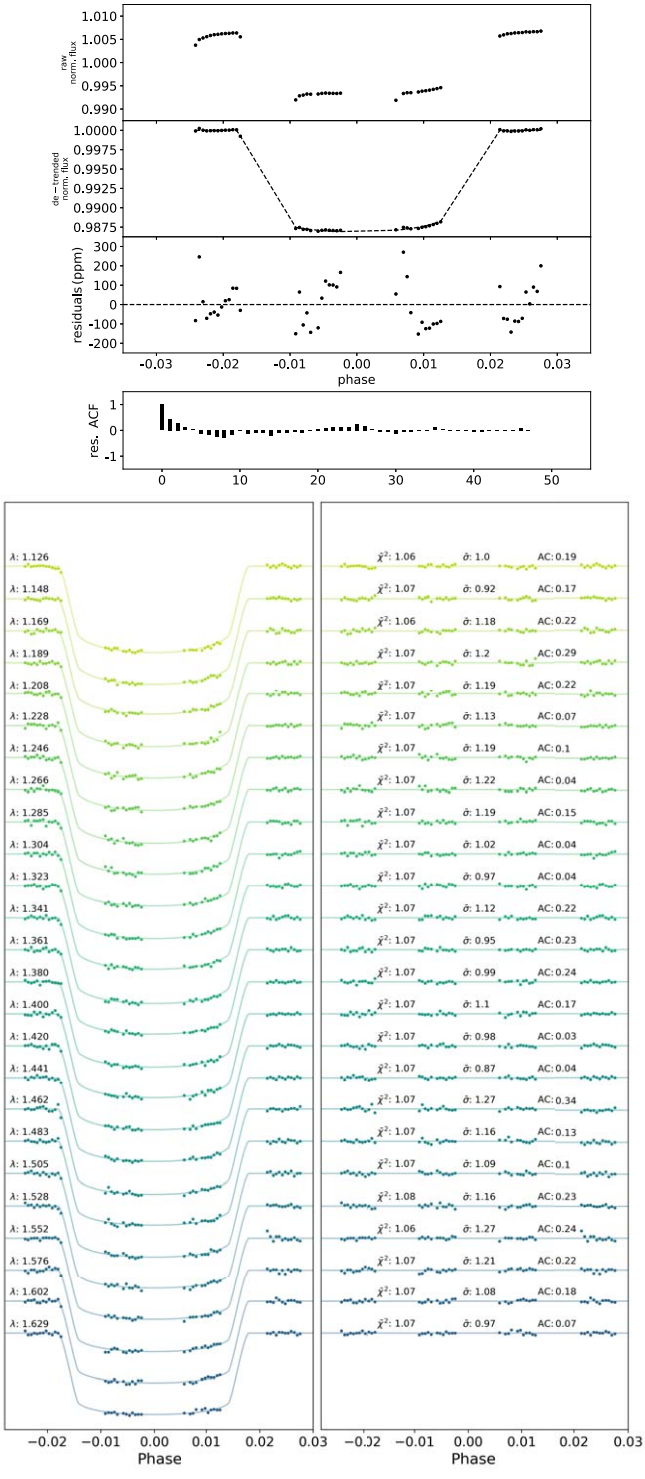

Figure 4. Top figure: results of the white-light curve of WASP-62 b. Top: raw light curve, after normalization. Second: light curve, divided by the best-fit model for the systematics. Third: residuals. Bottom: autocorrelation function of the residuals. Bottom figure: spectral light curves fitted with`Iraclis`for the transmission spectra where, for clarity, an offset has been applied. Left: the detrended spectral light curves with best-fit model plotted. Right: residuals from the fitting with values for the Chi-squared (χ^2), the standard deviation of the residuals with respect to the photon noise ($\bar{\sigma}$), and the autocorrelation (AC).

to vary freely between 10^{-12} and 10^{-1} in volume mixing ratio. The planetary radius was set to vary in our models between 0.5 $R_{\rm ref}$ and 1.5 $R_{\rm ref}$, where $R_{\rm ref}$ is the reference radius from the literature for each planet, as shown in Table 1. This is assumed to be equivalent to the radius at 10^6 Pa pressure.

The cloud-top pressure ranged from 10^{-2} to 10^6 Pa, in log-uniform scale. We consider a cloud-top pressure of 10^6 Pa to be

Table 3
Table of Fitted Parameters for the Retrievals Performed on Our Targets

Retrieved Parameters	Bounds	WASP-127 b	WASP-79 b	WASP-62 b
$\log(H_2O)$	1e−12-1e−1	$-2.71^{+0.78}_{-1.05}$	$-2.43^{+0.57}_{-0.76}$	$-2.03^{+0.52}_{-1.27}$
log(FeH)	1e−12-1e−1	$-5.25^{+0.88}_{-1.10}$	$-4.42^{+0.91}_{-1.18}$	$-3.04^{+2.18}_{-2.27}$
$\log(CH_4)$	1e−12-1e−1	<-5	<-5	<-5
log(CO)	1e−12-1e−1	<-3	<-3	<-3
$\log(CO_2)$	1e−12-1e−1	<-3	<-3	<-3
log(NH3)	1e−12-1e−1	<-5	<-5	<-5
T_p [K]	400-2500	1304^{+185}_{-175}	996^{+249}_{-228}	891^{+211}_{-164}
R_p [R_J]	± 50%	$1.15^{+0.04}_{-0.04}$	$1.55^{+0.02}_{-0.02}$	$1.35^{+0.01}_{-0.02}$
$\log(P_{clouds})$	1e−2-1e6	$1.7^{+0.93}_{-0.66}$	>4	$3.63^{+1.46}_{-1.29}$
μ (derived)		$2.34^{+0.20}_{-0.03}$	$2.38^{+0.33}_{-0.07}$	$2.39^{+0.51}_{-0.08}$
ADI	⋯	167.9	17.1	16.2
σ level	⋯	$>5\sigma$	$>5\sigma$	$>5\sigma$
		Updated Ephemeris		
P [days]	⋯	$4.1780619 \pm 1.3 \times 10^{-6}$	$3.66239344 \pm 3.5 \times 10^{-7}$	$4.41194014 \pm 7.4 \times 10^{-7}$
T_0 [BJD_{TDB}-2450000]	⋯	$8238.943367 \pm 5.5 \times 10^{-5}$	$8160.186968 \pm 3.9 \times 10^{-5}$	$8476.084602 \pm 4.0 \times 10^{-5}$

a cloud-free atmosphere; the gray cloud model used for this study corresponds to a fully opaque layer below the cloud-top pressure.

An isothermal atmosphere was assumed and the planetary temperature, T_p, set to vary from 400 to 2500 K; this is to accommodate the wide range in equilibrium temperatures between our three planets, which are between 1400 and 1750 K as shown in Table 1.

2.4. Atmospheric Detectability Index

To quantify the detection significance of an atmosphere, we use the Atmospheric Detectability Index (ADI) from Tsiaras et al. (2018), positively defined as the Bayes Factor between the nominal atmospheric model and the flat-line model (i.e., a model representing a fully cloudy atmosphere). For the flat-line model, the only free parameters are the planet radius and temperature, along with the cloud pressure. The nominal model then includes Rayleigh scattering and the CIA of H_2–H_2 and H_2–He, as well as molecular opacities. If an atmosphere is detected at the 3σ and 5σ level,s the corresponding ADI will be above 3 and 11, respectively. An ADI below 3 suggests the atmospheric detection is not significant, indicating the spectral feature amplitudes are insufficient given the uncertainty of the data.

To quantify the detection of particular species, we computed the Bayes factor, which is the ratio of the Bayesian evidences of different models. We follow the formalism by Kass & Raftery (1995) for model selection significance as well as translate the Bayes factor to the more traditional σ significance nomenclature following Benneke & Seager (2012).

2.5. Ephemeris Refinement

Accurate knowledge of exoplanet transit times is fundamental for atmospheric studies. To ensure the planets studied here can be observed in the future, we used our HST white-light curve midtimes, along with data from TESS (Ricker et al. 2014), to update the ephemeris of each planet. TESS data is publicly available through the MAST archive, and we used the pipeline from Edwards et al. (2020b) to download, clean, and fit the 2 minute cadence data. WASP-127 b had been studied in Sector 9, WASP-79 b in Sectors 4 and 5, and WASP-62 b in Sectors 1–4 and 6–13. After excluding bad data, we recovered 4, 12, and 60 transits for WASP-127 b, WASP-79 b, and WASP-62 b, respectively. These were fitted individually with the planet-to-star radius ratio R_p/R_s, reduced semimajor axis (a/R_s), inclination (i), and transit midtime (T_{mid}) as free parameters. Finally, we fitted a linear period (P) to these midtimes and selected the updated transit midtime (T_0) such that the covariance between T_0 and P was minimized. Midtimes were converted to BJDTDB using the tool from Eastman et al. (2010).

3. Results

Each planet's retrieval produced results consistent with the significant presence of water vapor, with opaque clouds in two of the three planets. While we did attempt to retrieve the carbon-based molecules, CO, CO_2, and CH_4, only their upper value could be constrained as they lack strong absorption features in the G141 wavelength range. In each case, our best-fit solution also indicates the presence of FeH, with abundances of log(FeH) between −3.04 and −5.25.

The relatively high water abundances retrieved (10^{-2}–10^{-3}) for these three planets can be suggestive of metallicities in the super-solar regime (Madhusudhan 2012; Charnay et al. 2018; Pinhas et al. 2018). However, there are known degeneracies between the the cloud pressure, 10^6 Pa radius, and water abundance retrieved from WFC3 data (Griffith 2014; Heng & Kitzmann 2017). Additionally, due to the restrictions of the WFC3 wavelength ranges, these observations are not generally sensitive to the main carbon-bearing species, and arguments of high metallicities are usually based on retrieved water abundances alone, assuming that half of the oxygen is in H_2O as expected for a solar C/O ratio at high temperatures (Madhusudhan 2012). Hence, observations covering longer wavelength ranges are needed to further constrain the C/O ratios of these planets, to fully understand their metallicity.

Our findings are shown in Table 3, with Figure 5 showcasing all three retrieved spectra with the corresponding contributions for each opacity source in Figure 6. For WASP-127 b, the

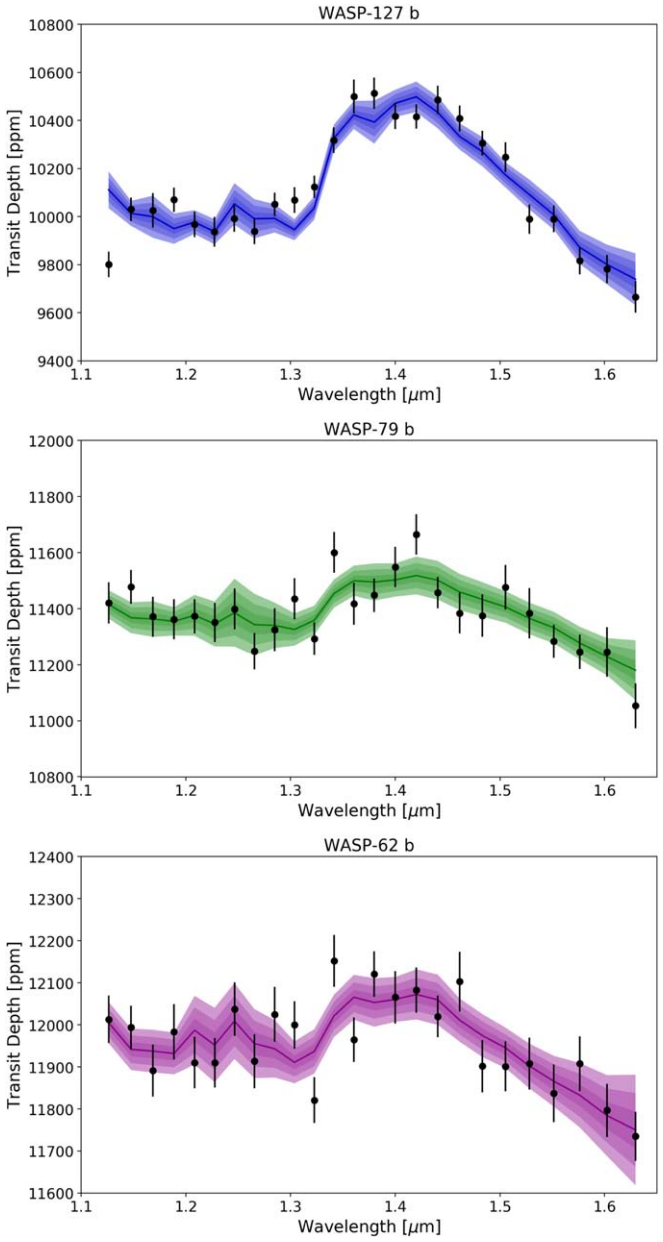

Figure 5. WFC3 spectral data and best-fit models, with 1σ–3σ uncertainties, for the three planets: from top to bottom, WASP-127 b, WASP-79 b, and WASP-62 b.

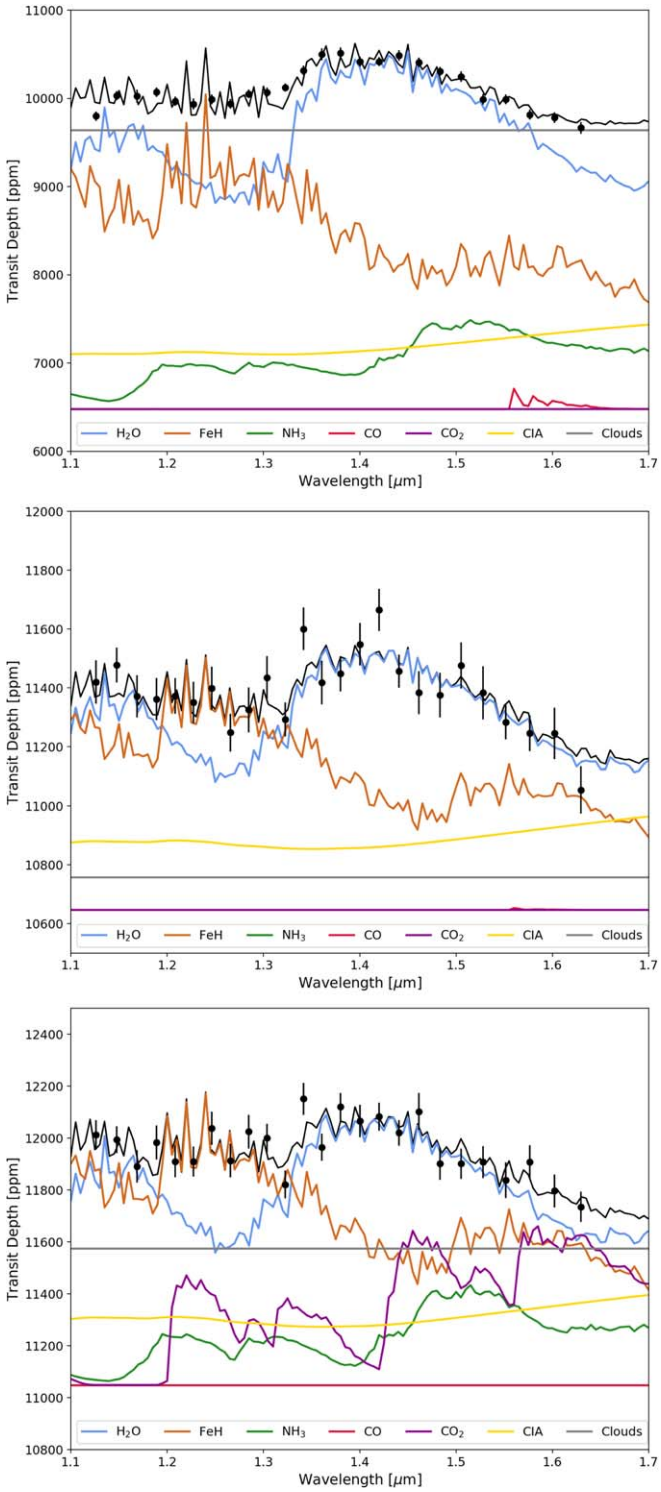

Figure 6. WFC3 spectral data and the contributions of active trace gases and clouds from the best-fit model for each planet. Top: WASP-127 b. Middle: WASP-79 b. Bottom: WASP-62b. In each case, the black line denotes the best-fit model.

posteriors are shown in Figure 7, with equivalent results for WASP-79 b in Figure 8 and for WASP-62 b in Figure 9.

3.1. WASP-127 b

As expected given the low density, we retrieved a statistically significant atmosphere around WASP-127 b with a strong detection of water and opaque clouds. The retrieved radius is $1.16^{+0.04}_{-0.04}$ R_J at a pressure of 10 bar, which is smaller than stated in previous studies (1.37 R_J; Chen et al. 2018). However, our analysis is best fit with high-altitude opaque clouds ($\log(P_{clouds}) = 1.85^{+0.97}_{-0.66}$ Pa), which corresponds to approximately 1.37 R_J, thus explaining this difference between the retrieved radius and the radius in the literature.

In terms of chemistry, our best-fit solution indicates significant amounts of water at $\log(H_2O) = -2.71^{+0.78}_{-1.05}$ and constraints on FeH. FeH produces a flat absorption between 1.2 and 1.3 μm, while deepening the slope in the longer wavelengths (around 1.5–1.6 μm). We also note a correlation between the amount of these two molecules, the radius, and the cloud pressure. For less H_2O and FeH, the model requires deeper clouds, but a higher base planet radius. In particular, the abundance of FeH can vary from 10^{-4} to 10^{-7}, depending the complementary contribution of clouds.

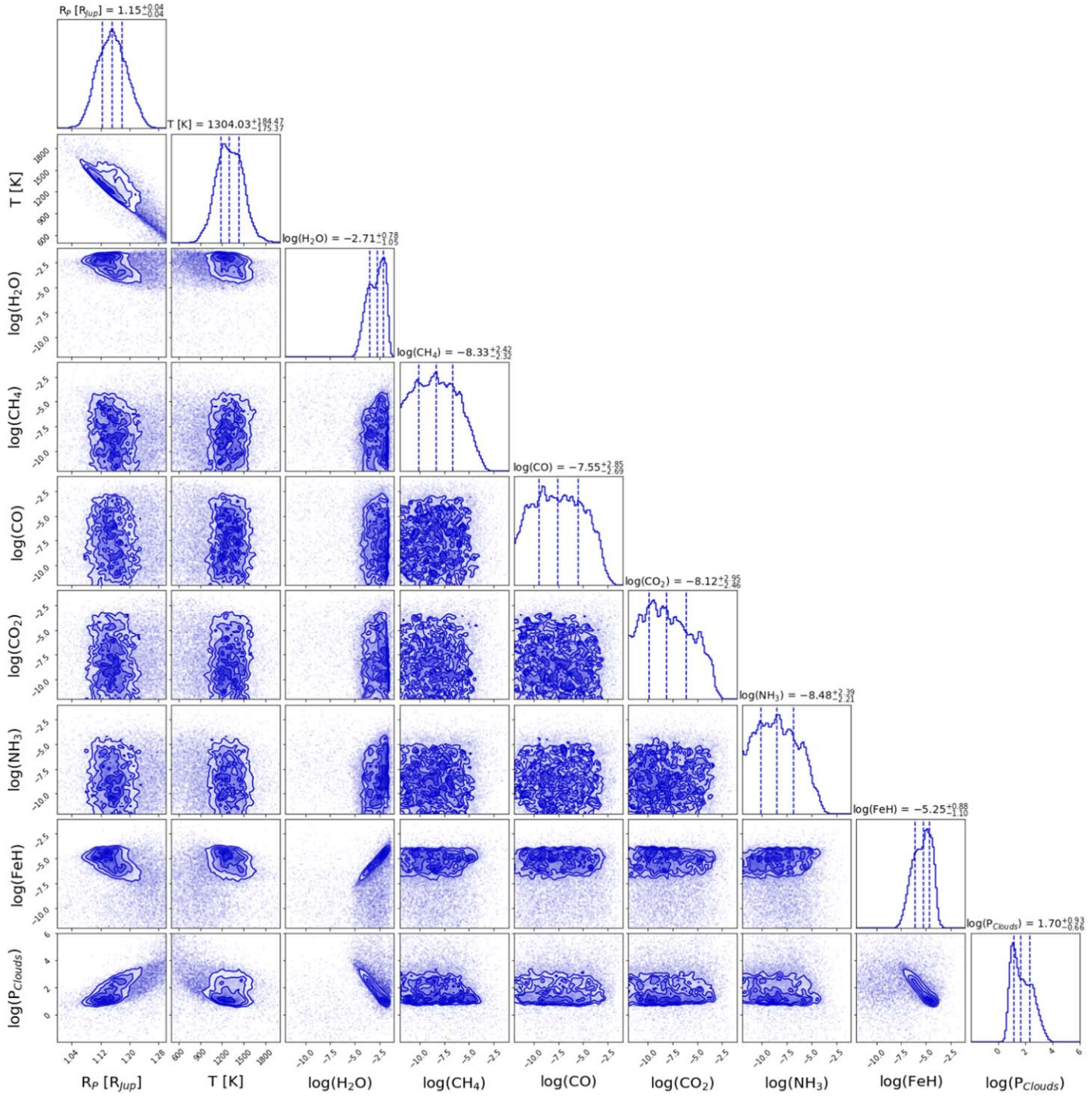

Figure 7. Posterior distributions from our WASP-127 b retrieval. The corresponding posteriors for WASP-79 b and WASP-62 b are in the appendix (Figures 8 and 9).

The posteriors for FeH are, however, always distinct; clouds cannot be used to completely replace the additional visible absorption provided by FeH. A lower metallicity, and larger radius, could be consistent with current data, but is not the best-fit solution. Given the posterior distribution, we do not find a clear correlation between the radius and the water abundance.

3.2. WASP-79 b

For WASP-79 b, we get very similar results to those of WASP-127 b, with the exception of the cloud deck. Following our baseline approach, we find a large abundance of water at $\log(H_2O) = -2.43^{+0.57}_{-0.76}$ and well-defined constraints on the abundance of FeH with $\log(FeH) = -4.42^{+0.91}_{-1.18}$. The clouds, however, do not impact the model, and we only retrieve a lower limit on their top pressure ($P_{clouds} > 10^3$ Pa). This means that either the planet possesses a clear atmosphere, or that the clouds are located below the visible pressure, at which the atmosphere is opaque due to molecular or CIA. We do not detect signatures of CH_4, CO, or CO_2. The retrieved temperature of $\sim$1000 K is lower than the calculated equilibrium temperature for this type of planet; this was also found in Sotzen et al. (2020) and is discussed further in Section 4.

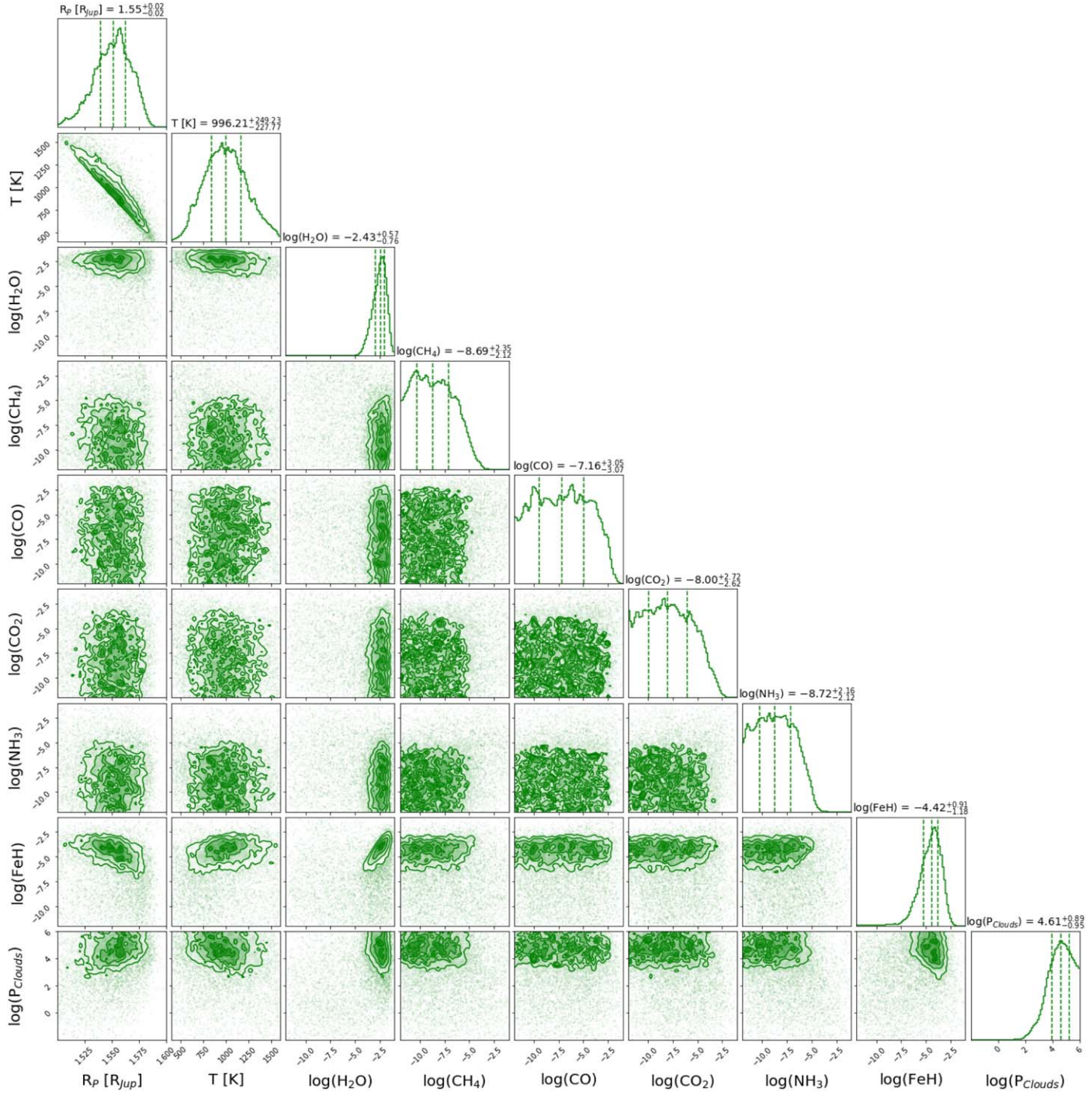

Figure 8. Posterior distributions for WASP-79 b.

3.3. WASP-62 b

The recovered spectrum of WASP-62 b was flatter than that of the two other planets. However, we found that the data were best explained by the presence of H_2O and FeH and, for this retrieval, the recovered abundances are $\log(H_2O) = -2.03^{+0.52}_{-1.27}$ and $\log(FeH) = -3.04^{+2.18}_{-2.27}$. These results stem from detections in the lower-wavelength spectrum, below 1.5 μm, which guides the retrieval toward non-fully opaque sources, such as clouds and high-radius solutions. Again, the retrieved temperature is lower than the expected 1475 K equilibrium temperature, which is indicative of a large day–night temperature contrast and/or efficient cooling mechanisms. Our analysis indicates that clouds are likely to be present, but the quality of our data means that we cannot completely rule out a clear atmosphere.

The retrieved abundances are very high, but we note that the posteriors allow for a wide range of abundances and present interesting correlations, such as, the lower the abundances of H_2O and FeH are, the higher in the atmosphere the clouds are located. There is also a negative correlation between the molecular abundances and the temperature and, from the posterior distributions, we see that the data are consistent with abundances of order of 10^{-4} in H_2O and FeH.

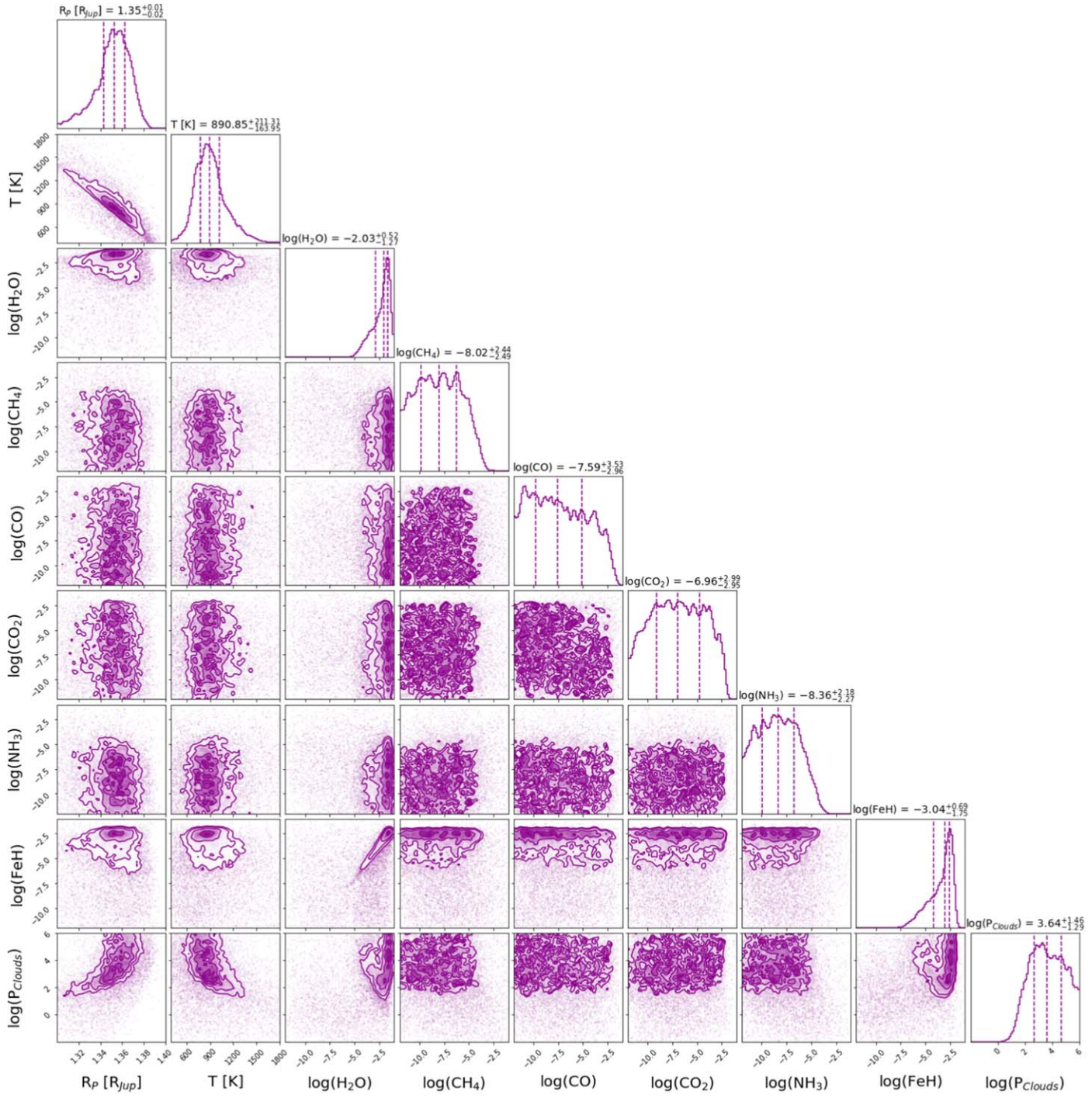

Figure 9. Posterior distributions for WASP-62 b.

Finally, we note that given the low spectral variations in this spectrum, the retrieval may lack a scale height constraint, which would provide a relevant baseline in predicting the molecular abundances and temperature more accurately.

3.4. Ephemeris Refinement

We found that the observed HST and TESS transits were consistent with literature ephemeris within 1σ. Nevertheless, we refined the period and reference midtransit time for each planet. The updated ephemeris is given in Table 3 while the fitting for the TESS data can be seen in the figures of the Appendix. The transit depth and errors of the WFC3 for the three planets are presented in Table 4. The observed minus calculated plots are given in Figure 10, and all transit midtimes used for the fitting are listed in two tables in the Appendix. These have been uploaded to ExoClock,[21] an initiative to ensure transiting planets are regularly followed up, keeping their ephemeris up to date for the ESA Ariel mission (Tinetti et al. 2018).

4. Discussion

Initially, our baseline model did not include FeH, but these models struggled to fit the data, forcing solutions to lower

[21] https://www.exoclock.space

Table 4
WFC3 Transit Depths and Errors (in ppm) for WASP-127 b, WASP-79 b, and WASP-62 b

Wavelength	WASP-127 b	WASP-79 b	WASP-62 b
1.12625	9800 ± 53	11420 ± 74	12012 ± 56
1.14775	10030 ± 48	11477 ± 59	11993 ± 51
1.16860	10026 ± 72	11371 ± 71	11890 ± 61
1.18880	10070 ± 50	11362 ± 71	11983 ± 65
1.20835	9967 ± 53	11372 ± 61	11909 ± 61
1.22750	9936 ± 61	11350 ± 70	11909 ± 58
1.24645	9990 ± 54	11398 ± 72	12036 ± 64
1.26550	9938 ± 53	11248 ± 64	11913 ± 64
1.28475	10050 ± 49	11325 ± 76	12024 ± 65
1.30380	10068 ± 52	11434 ± 73	11999 ± 56
1.32260	10123 ± 46	11292 ± 58	11820 ± 54
1.34145	10318 ± 53	11600 ± 72	12151 ± 61
1.36050	10500 ± 70	11417 ± 74	11964 ± 52
1.38005	10513 ± 65	11448 ± 59	12120 ± 53
1.40000	10417 ± 53	11548 ± 72	12065 ± 62
1.42015	10415 ± 50	11664 ± 71	12082 ± 54
1.44060	10485 ± 59	11457 ± 56	12019 ± 49
1.46150	10408 ± 54	11384 ± 73	12102 ± 71
1.48310	10305 ± 51	11375 ± 75	11901 ± 62
1.50530	10246 ± 61	11476 ± 78	11901 ± 59
1.52800	9989 ± 60	11383 ± 89	11907 ± 61
1.55155	9990 ± 55	11283 ± 58	11837 ± 68
1.57625	9816 ± 56	11245 ± 61	11907 ± 65
1.60210	9781 ± 58	11245 ± 87	11796 ± 63
1.62945	9665 ± 65	11053 ± 80	11734 ± 58

temperatures and nonphysical values in order to account for the opacity sources at shorter wavelengths with a gray cloud deck. FeH has strong absorption features in the visible and near-infrared, and can be expected at the temperatures of these planets (Madhusudhan et al. 2016; Tennyson & Yurchenko 2018); hence, we propose it as the possible absorber to suit our spectral features and explore our justifications for FeH over molecules with similar spectral signatures, such as TiO or VO, in this discussion. FeH was not included in the analysis of Tsiaras et al. (2018) and thus, for the hotter planets in that study, retrievals with FeH may alter the retrieved atmospheric characteristics.

Theoretical equilibrium chemistry models predict FeH (Sharp & Burrows 2007; Woitke et al. 2018) to be stable in the gas phase at the temperatures and pressures consistent with the planetary atmospheres considered here. FeH has previously been observed in L and M brown dwarfs at 1800 K (Visscher et al. 2010). In cooler T dwarfs, it has been shown to appear where brown dwarfs have temperatures below 1350 K (Burgasser et al. 2002), with some additional studies (Cushing et al. 2008) confirming FeH detection in dwarfs with temperatures of 1000 K. The latter of these detections is at temperatures comparable to the retrieved temperatures of the planets here.

A recent study from Ehrenreich et al. (2020) found atomic iron (Fe) in the dayside of the planet WASP-76 b and not in the terminator, concluding that Fe is condensing on the nightside, then falling into deeper layers of the atmosphere. Furthermore, the results in Pluriel et al. (2020) and Caldas et al. (2019) have investigated how the 3D structure of the atmosphere biases the abundances retrieved with typical retrieval codes, as there is a chemical dichotomy between the day- and nightside that is not considered in a 1D treatment of transit geometry.

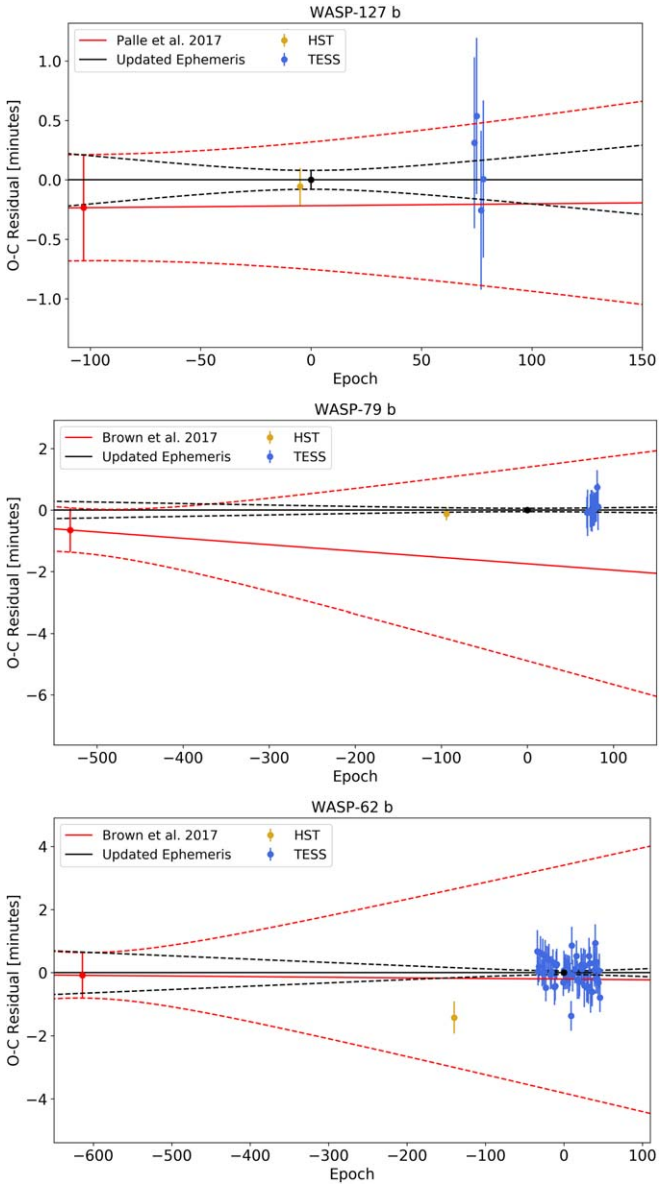

Figure 10. Observed minus calculated ($O - C$) transit midtimes for WASP-127 b (top), WASP-79 b (middle), and WASP-62 b (bottom). Transit midtime measurements from this work are shown in gold (HST) and blue (TESS), while literature T_0 values are in red. The black line denotes the new ephemeris of this work, with the dashed lines showing the associated 1σ uncertainties and the black data point indicating the updated T_0. For comparison, the previous literature ephemeris and their 1σ uncertainties are given in red. In all cases, our results are compatible with the literature but provide a further refinement of the ephemeris.

We therefore identify three possible scenarios for the detection of FeH in these planets:

- FeH is originating from the dayside where the temperature is much higher and leaks in the nightside before it is able to condense due to circulation processes (Heng et al. 2011).
- Atmospheric retrieval studies involve temperature bias due to 3D effects, and we indeed retrieve a cooler temperature than expected; we discuss this in Section 4.1.
- A 3D effect is in play, and we retrieve the FeH in the dayside inflated region of the limb (Caldas et al. 2019; Pluriel et al. 2020).

Table 5
Comparison of the Bayesian Log Evidence for Different Models

WASP-127 b (No Molecules Log Evidence: 1.73—Model (1))				
Setup	Log Evidence	Sigma	Retrieved Temperature [K]	Equilibrium Temperature [K]
(2) H_2O, clouds	161.87	>7 w.r.t. (1)	1027	1400[†]
(3) H_2O, CH_4, CO, CO_2, NH3, clouds	161.27	<1 w.r.t. (2)	1005	
(4) H_2O, FeH, clouds	170.20	4.48 w.r.t. (2)	1305	
(5) H_2O, CH_4, CO, CO_2, NH3, FeH, clouds	169.65	4.49 w.r.t. (3)	1304	
WASP-79 b (No Molecules Log Evidence: 173.33—Model (1))				
Setup	Log Evidence	Sigma	Retrieved Temperature [K]	Equilibrium Temperature [K]
(2) H_2O, clouds	187.77	5.72 w.r.t. (1)	627	1716[‡]
(3) H_2O, CH_4, CO, CO_2, NH3, clouds	187.88	<1 w.r.t. (2)	618	
(4) H_2O, FeH, clouds	191.16	3.09 w.r.t. (2)	948	
(5) H_2O, CH_4, CO, CO_2, NH3, FeH, clouds	190.73	2.89 w.r.t. (3)	996	
WASP-62 b (No Molecules Log Evidence: 176.35—Model (1))				
Setup	Log Evidence	Sigma	Retrieved Temperature [K]	Equilibrium Temperature [K]
(2) H_2O,clouds	187.22	5.03 w.r.t. (1)	618	1475[‡]
(3) H_2O, CH_4, CO, CO_2, NH3, clouds	186.66	<1 w.r.t. (2)	566	
(4) H_2O, FeH, clouds	192.59	3.72 w.r.t. (2)	890	
(5) H_2O, CH_4, CO, CO_2, NH3, FeH, clouds	192.31	3.80 w.r.t. (3)	891	

[†] Lam et al. (2017) [‡] Brown et al. (2017)

Note. For WASP-79 b and WASP-62 b, the retrieved temperature is always significantly below the equilibrium temperature for the planet, particularly if FeH is not included as an opacity source. In all cases, a better fit is obtained by including FeH.

Table 5 contains the log evidence of several retrievals for each planet. In all cases, the addition of FeH increases the goodness of fit while also raising the retrieved temperature. We note that all models included clouds. By comparing the log evidence of the models with only H_2O and the models with H_2O and FeH, we confirm for all planets that clouds are not a suitable opacity substitute for FeH.

The difference in log evidence for these models ($\Delta \log(E)$) is 8.33, 3.39, and 5.37 for WASP-127 b, WASP-79 b, and WASP-62 b respectively (4.48σ, 3.09σ, and 3.72σ detection of FeH, respectively). This indicates strong to decisive evidence in favor of models containing FeH (Kass & Raftery 1995; Benneke & Seager 2012; Changeat et al. 2019).

While we postulate that our evidence holds for FeH, it is possible that we detect another, yet unidentified, opacity source with absorption characteristics similar to those of FeH over the WFC3 passband. For instance, similar absorption features can be produced with metal oxides such as TiO, VO, and YO. However, we do not expect the presence of these molecules in these planets due to the planets' low equilibrium temperatures. TiO and VO have condensation temperatures of over ~2000 K (Lodders 2002; Hubeny et al. 2003; Fortney et al. 2008); the highest equilibrium temperature featured of these three planets is WASP-79 b's 1716 K, as referenced in Table 1, thus rendering it less likely that the spectral features are due to TiO and VO compared to FeH. Ultimately, this further exemplifies the need for longer wavelength coverage with JWST or Ariel to confirm the nature of observed absorption in the future.

For each planet, we have calculated the ADI and found significant evidence of atmospheric features for all three. Given the water detection on all three planets, our results support the conclusions drawn by Tsiaras et al. (2018); inflated, hot Jupiter-like planets do not necessarily destroy water in their upper atmospheres.

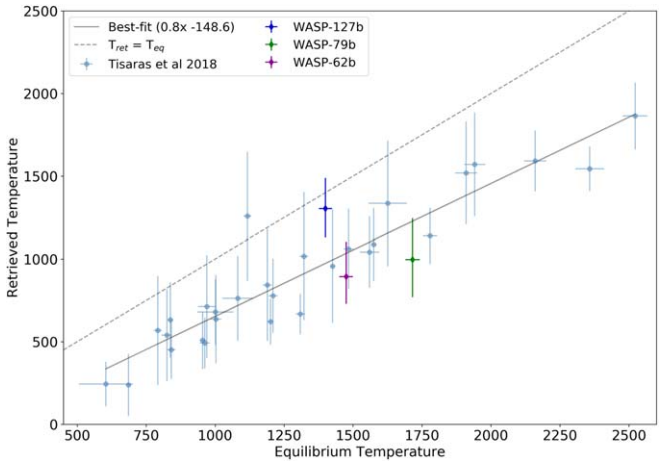

Figure 11. Correlation between the retrieved temperature and the equilibrium temperature for the planets studied in Tsiaras et al. (2018). We observe a global trend wherein the retrieved temperature is lower than the calculated equilibrium temperature and derived a best fit for this trend. WASP-127 b, WASP-79 b, and WASP-62 b have been added; we can see that they follow this trend as well.

4.1. Retrieved Temperature

For the three planets considered, the temperature retrieved is notably lower than the equilibrium temperature. In Figure 11, we present a plot analyzing the temperatures retrieved for other planets, particularly giving attention to the population paper we based our study on, Tsiaras et al. (2018). Indeed, retrieved temperatures are typically lower than the equilibrium ones, and we derived a best fit of this.

One of the key assumptions leading to this effect is that the equilibrium temperature is usually calculated for the planet dayside and considering a planetary albedo of zero. Considering

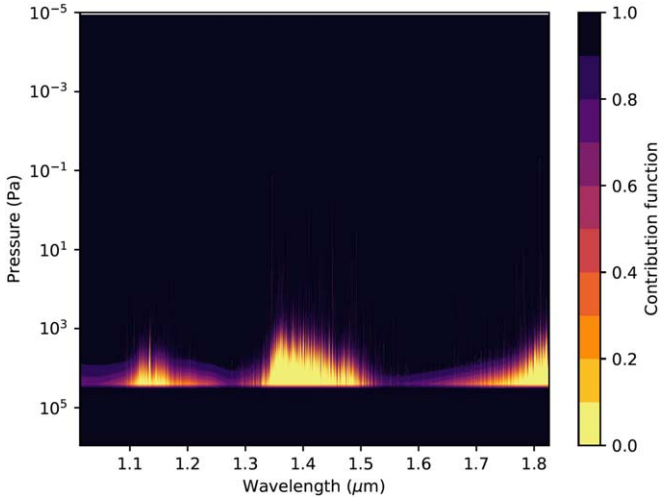

Figure 12. Typical contribution function of our retrievals. We can see the effect of the H_2O lines. The rise in sensitivity at $\approx 10^4$ Pa is due to the opaque cloud.

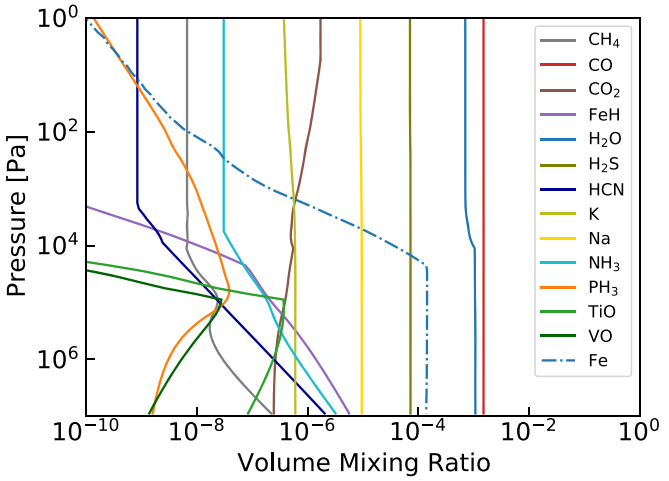

Figure 13. Expected abundances of WASP-127 b generated by Exo-REM, assuming chemical nonequilibrium for C-, N-, and O-bearing species; an eddy diffusion coefficient of 10^8 cm^2 s^{-1}; and a metallicity of three times solar (Lodders 2019). We have included TiO and VO to the Exo-REM run but found their predicted abundances to be negligible ($<10^{-14}$).

an albedo greater than zero necessarily implies a loss of energy and therefore a lower equilibrium temperature.

Furthermore, the region probed during transit eclipse observations is the terminator region: a mix between the day- and the nightside. The temperature difference observed may indicate a bias in the retrievals, which consider exclusively a 1D geometry of the atmospheres. This bias has been pointed out by several studies, especially Caldas et al. (2019), MacDonald et al. (2020), and Pluriel et al. (2020).

4.2. WASP-127 b

We used Exo-REM (Exoplanet Radiative-convective Equilibrium Model; Baudino et al. 2015; Charnay et al. 2018), a self-consistent simulation software for brown dwarfs and giant exoplanets, to calculate the mean temperature profile and the expected abundances of WASP-127 b assuming a solar composition.

The model suggests significant abundances of H_2O, CO, and Na; though, as stated previously, the WFC3 coverage means our data set is only sensitive to H_2O.

From Figure 12, we can see that our retrieval is sensitive at pressures between $\approx 10^4$ and 10^2 Pa. Figure 13 indicates that the retrieved abundances of WASP-127 b are compatible with a solar composition in this pressure range. The mean retrieved abundance of FeH is higher than expected values; however, the error spans three orders of magnitude, allowing for more physical solutions, as discussed at the beginning of this section.

As displayed in Figure 14, the retrieved temperature of WASP-127 b is compatible with the calculated mean temperature profile within our pressure sensitivity range. We can also see that the calculated temperature profile crosses the condensation curves of MnS and Cr between 10^4 and 10^3 Pa. We could therefore expect clouds composed of these species to form at these pressures.

Low- and high-resolution spectra of WASP-127 b have been collected with ground-based instruments. Palle et al. (2017) obtained low-resolution spectroscopy with the Andalucia Faint Object Spectrograph and Camera (ALFOSC) spectrograph mounted on the Nordic Optical Telescope (NOT), covering the spectral range 0.45–0.85 μm. A slope was detected in the optical

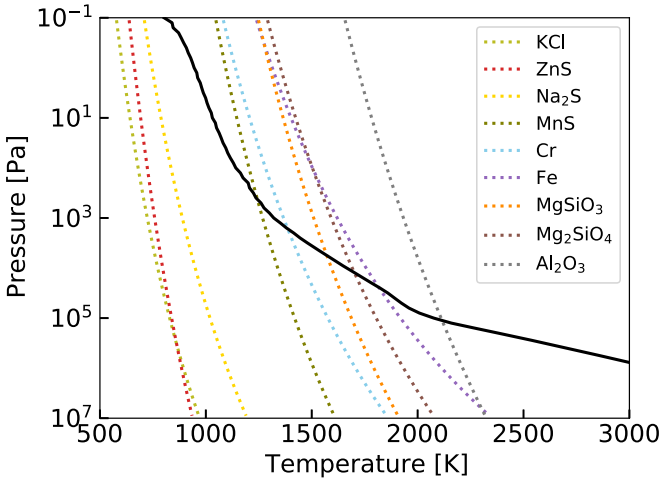

Figure 14. Mean temperature profile of WASP-127 b, assuming radiative transfer equilibrium, generated by Exo-REM. The condensation profiles of various species are represented as dotted lines.

wavelength spectrum, interpreted as Rayleigh scattering and potentially Na. They also attribute the trend to TiO/VO with low significance. Chen et al. (2018) observed with the OSIRIS spectrograph, mounted on the Gran Telescopio Canarias (GTC) telescope, covering the range 0.4–1.0 μm. They presented detection of alkali metals (Na, K and Li) and hints of clouds and water with a retrieved abundance of $\log(H_2O) = -2.60^{+0.94}_{-4.56}$. A recent study with the HST STIS and WFC3, combined with Spitzer data from IRAC 1 and 2, also concluded that water was present in the atmosphere. Spake et al. (2020) used a Markov Chain Monte Carlo model to fit the data, resulting in a best-fit solution detecting H_2O, CO_2, Na, and K; their water abundance of $\log(H_2O) = -2.87^{+0.58}_{-0.61}$ is similar to the value retrieved here.

Hence, our independent data reduction and analysis of the water content in the atmosphere of WASP-127 b is consistent with these studies. We do not attempt a joint retrieval with this data due to the potential incompatibility between the data sets from different instruments as highlighted in Yip et al. (2019).

Given that the planet lies within the short-period Neptunian desert and has large atmospheric features, it will be an intriguing target for further characterization.

4.3. WASP-79 b

Sotzen et al. (2020) utilized the same WFC3 data set, along with observations from ground-based facilities, TESS, and Spitzer, to study the atmosphere of WASP-79 b. Their retrieval results indicates the presence of H_2O, Na, and FeH. Our retrieved water abundance is consistent with that from Sotzen et al. (2020): $(-2.20 < \log(H_2O) < -1.55)$.

In our retrievals without FeH as an opacity source, our solution is driven to low temperatures; Sotzen et al. (2020) encountered a similar predicament when attempting to fit a chemical equilibrium model to the data. Here, by adding FeH as a retrieval parameter, our recovered temperature increases to 996^{+249}_{-228} K, which more readily agrees with what is expected for the terminator region.

While the temperature is still cooler than expected, we note the degeneracy with the 10 bar radius. Our analysis of purely the HST/WFC3 data also favors the presence of H_2O and FeH. Na does not have features within the WFC3 spectral range, and we do not attempt the addition of other data for the aforementioned reasons.

4.4. WASP-62 b

WASP-62 b has demonstrably similar bulk characteristics to HD 209458b; both planets have roughly the same radius and effective temperature, although HD 209458b is ≈20% more massive than WASP-62 b (Bonomo et al. 2017). Given their similarities, we may expect them to exhibit a similar atmospheric chemistry and structure. HD 209458b has been extensively analyzed in the literature, with 3D simulations (Showman et al. 2009) and cloud analysis (Sing et al. 2016), making it ideal to interpret the results on WASP-62 b. We observe a cloud deck located at $\approx 2.5 \times 10^3$ Pa. This cloud deck could be explained by the condensation of $MgSiO_3$ in the atmosphere, as was the case with HD 209458b (Sing et al. 2016).

Using the models of Showman et al. (2009) and Caldas et al. (2019), we may expect the temperature at the terminator to be close to ≈1350 K. This is somewhat hotter than the 891^{+211}_{-164} K retrieved in our standard setup (2.2σ). However, as seen in the posterior plot in Figure 9, there is a strong correlation between the temperature, the planet radius, and the cloud pressure; thus, the data remain consistent with the expected temperature.

4.5. Future Characterization

Upcoming ground and space-based telescopes such as the European Extremely Large Telescope (E-ELT; Brandl et al. 2018), the Thirty Meter Telescope (TMT; Skidmore et al. 2018), the Giant Magellan Telescope (GMT; Fanson et al. 2018), the JWST (Greene et al. 2016), Twinkle (Edwards et al. 2018), and Ariel (Tinetti et al. 2018) will characterize the atmospheres of a large population of exoplanets via transit and eclipse spectroscopy at visible and infrared wavelengths. These missions will move the exoplanet field from an era of detection into one of characterization, allowing for the identification of the molecular species present and their chemical profile, insights into the atmospheric temperature profile, and the detection and characterization of clouds (e.g., Rocchetto et al. 2016; Rodler 2018; Changeat et al. 2019).

Ariel has been selected as ESA's M4 mission adoption candidate for launch in 2028 and is designed for the characterization of a large and diverse population of exoplanetary atmospheres to provide insights into planetary formation and evolution within our Galaxy. Ariel will provide simultaneous photometry and spectroscopy over 0.5–7.8 μm. Each of the planets studied here is an excellent target for atmospheric studies with Ariel (Edwards et al. 2019), and we use ArielRad (Mugnai et al. 2020) to simulate observations of this forthcoming mission. For each of the planets, we take the best-fit solution from the Hubble WFC3 analysis to model Ariel observations at the native resolution of its instruments. Figure 15 highlights the increased wavelength coverage and data quality that will be achieved with Ariel, allowing for a deeper understanding of each of these worlds. WASP-79 b is part of the JWST Early release Science program and will be observed by JWST with several different instruments (Bean et al. 2018). Here, we simulate JWST observations for these planets, assuming NIRISS GR700XD and NIRSpec G395H are used. Again, the increase in data quality is easily discernible and, although it is not a dedicated exoplanet mission, JWST promises to provide exquisite data for atmospheric characterization.

5. Conclusion

We have presented the analysis of data from Hubble's WFC3 G141 grism for three planets. By using the `Iraclis` pipeline and fitting the resultant spectra with TauREx, we have characterized the atmospheres of WASP-127 b, WASP-79 b, and WASP-62 b, recovering best-fit models that favor the presence of H_2O and FeH in each case. This was performed during the ARES Summer School, using software and data publicly available to the community in order to allow for reproducible results.

The properties of WASP-127 b, particularly its extended atmosphere with clouds and large spectral features; the resultant high atmospheric detectability; and its unusually low density; make it an ideal target for further characterization with the next generation of facilities. Large spectral features were also detected in WASP-79 b and WASP-62 b, with clouds in the atmosphere of the latter.

None of the three planets studied have strong features in their spectra that can be linked to NH_3, CH_4, CO, or CO_2. This is expected, given that their spectroscopic lines do not have major bands in this wavelength range compared to the H_2O and FeH lines and higher quality data, with a broader spectral coverage, is required to improve constraints on the atmospheric chemistry. Nevertheless, studying the atmospheric composition of these planets has extended the catalog of hot Jupiters studied with WFC3 from those by Tsiaras et al. (2018). The ADI introduced therein has been utilized effectively in this paper to estimate the significance of these atmospheric observations. This was done in order to unify the statistical results between our study and that of further populations studies, which remain fundamental tools in understanding the nature and evolutionary history of planets.

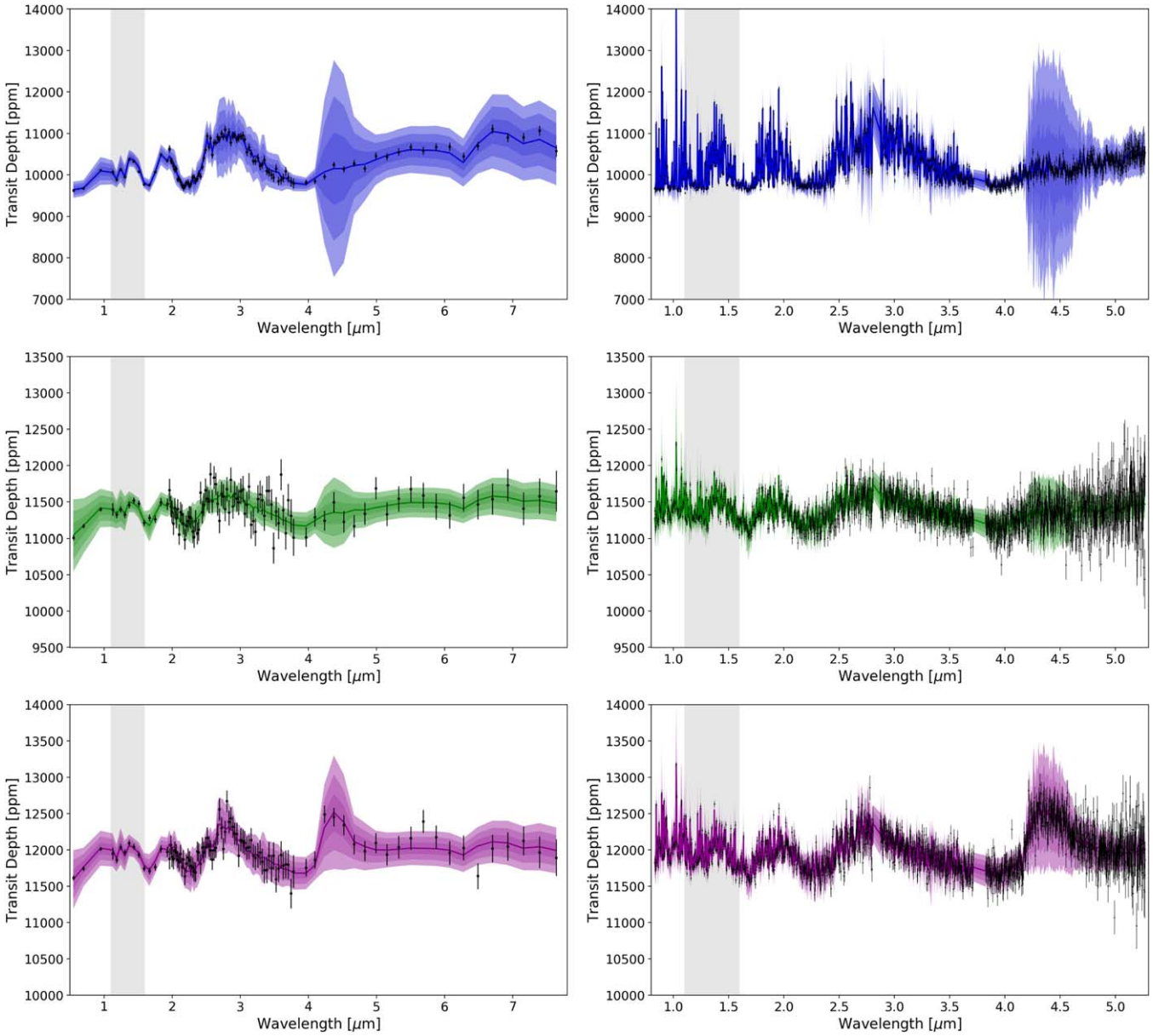

Figure 15. Simulated Ariel and JWST observations of the best-fit solutions retrieved in this work. For Ariel, WASP-127 b is for a single observation, while WASP-79 b and WASP-62 b have three stacked transits each. The transit depths have been offset to show the difference in the size of the atmospheric features between the planets. We note that, according to the work of Edwards et al. (2019), WASP-79 b and WASP-62 b may be more suited for study with Ariel via emission spectroscopy. JWST simulations have been performed using ExoWebb (B. Edwards et al. 2020, in preparation) for a single transit with NIRISS GR700XD as well as an observation with NIRSpec G395H.

We want to thank the anonymous reviewer for the insightful and constructive comments which helped improve the quality of the manuscript.

This work was realized as part of ARES, the Ariel Retrieval Exoplanet School, in Biarritz in 2019. The school was organized by Jean-Philippe Beaulieu with the financial support of CNES. J.P. B. acknowledges the support of the University of Tasmania through the UTAS Foundation and the endowed Warren Chair in Astronomy, Rodolphe Cledassou, Pascale Danto, and Michel Viso (CNES). B.E., Q.C., M.M., A.T., and I.W. acknowledge funding from the European Research Council (ERC) under the European Union's Horizon 2020 research and innovation program grant ExoAI (GA No. 758892) and STFC grants ST/P000282/1, ST/P002153/1, ST/S002634/1, and ST/T001836/1. N.S. acknowledges the support of the IRIS-OCAV, PSL. M.P. acknowledges support by the European Research Council under Grant Agreement ATMO 757858 and by the CNES. R.B. is a PhD fellow of the Research Foundation–Flanders (FWO). W.P., T.Z., and A.Y.J. have received funding from the European Research Council (ERC) under the European Union's Horizon 2020 research and innovation program (grant agreement No. 679030/WHIPLASH). O.V. thanks the CNRS/INSU Programme National de Planétologie (PNP) and CNES for funding support. G.G. acknowledges the financial support of the 2017 PhD fellowship program of INAF.

This paper includes data collected by the TESS mission, which is funded by the NASA Explorer Program. TESS data is publicly available via the Mikulski Archive for Space Telescopes (MAST).

Software: `Iraclis` (Tsiaras et al. 2016b), TauREx3 (Al-Refaie et al. 2019), pylightcurve (Tsiaras et al. 2016c), ExoTETHyS (Morello et al. 2020), ArielRad (Mugnai et al. 2020), ExoWebb (B. Edwards et al. 2020, in preparation), Astropy (Astropy Collaboration et al. 2018), h5py (Collette 2013),

emcee (Foreman-Mackey et al. 2013), Matplotlib (Hunter 2007), Multinest (Feroz et al. 2009), Pandas (McKinney 2011), Numpy (Oliphant 2006), SciPy (Virtanen et al. 2020).

Appendix

The white light curve_tting for the TESS data are in Figure 16 for WASP-127 b, Figure 17 for WASP-79 b, and Figure 18 for WASP-62 b. All transit mid times used for the fitting are listed in Table 6 and Table 7.

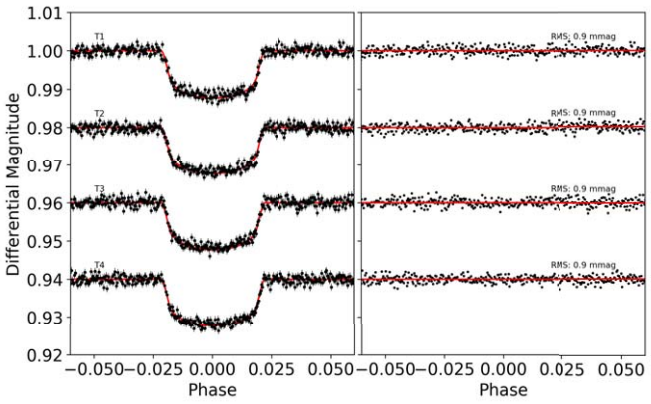

Figure 16. TESS observations of WASP-127 b presented in this work. Left: detrended data and best-fit model. Right: residuals from fitting.

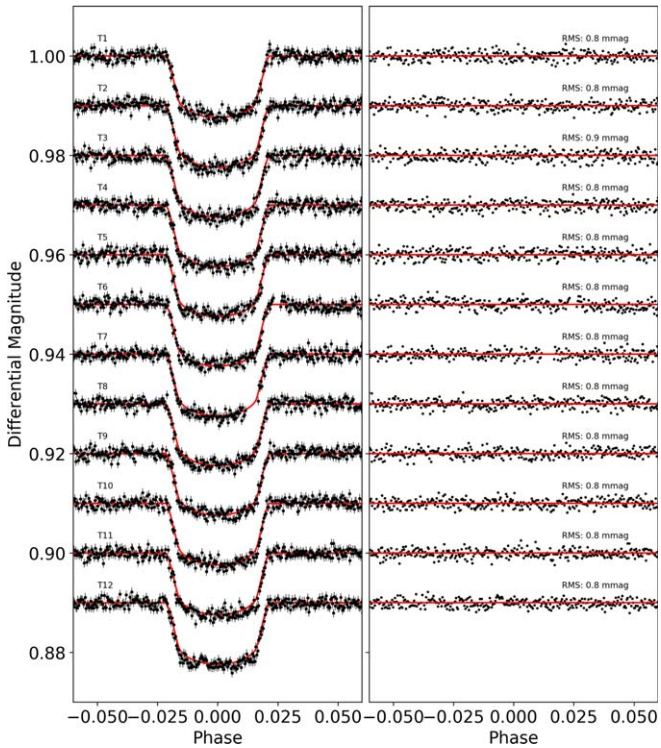

Figure 17. TESS observations of WASP-79 b presented in this work. Left: detrended data and best-fit model. Right: residuals from fitting.

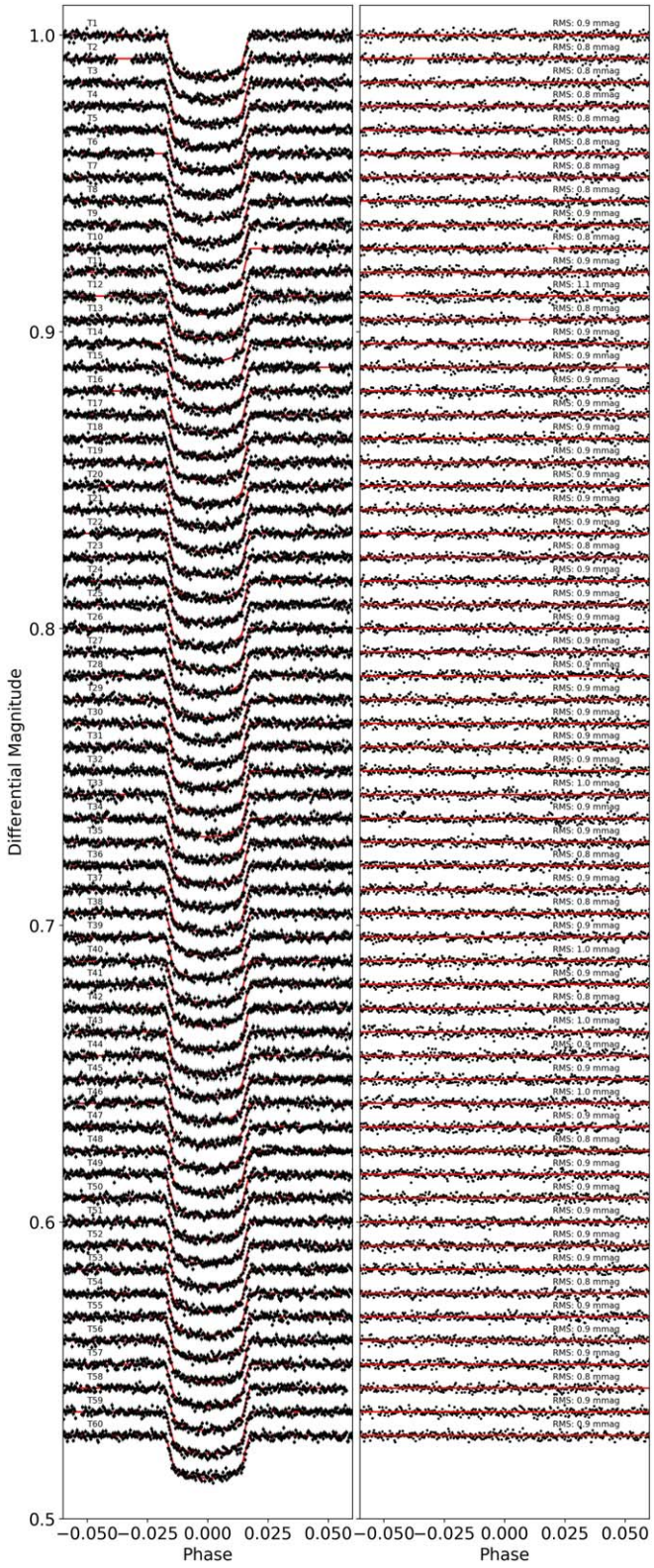

Figure 18. TESS observations of WASP-62 b presented in this work. Left: detrended data and best-fit model. Right: residuals from fitting.

Table 6
Transit Midtimes Used to Refine the Ephemeris of Planets from This Study

Planet	Epoch	Midtime [BJD_{TDB}]	References
WASP-127 b	−103	2457808.60283 ± 0.00031	Palle et al. (2017)
WASP-127 b	−5	2458218.053097 ± 0.000101	This Work*
WASP-127 b	74	2458548.11973 ± 0.000469	This Work
WASP-127 b	75	2458552.297636 ± 0.000428	This Work
WASP-127 b	77	2458560.65431 ± 0.000435	This Work
WASP-127 b	78	2458564.83219 ± 0.000431	This Work
WASP-79 b	−531	2456215.4556 ± 0.0005	Brown et al. (2017)
WASP-79 b	−94	2457815.92207 ± 0.000117	This Work*
WASP-79 b	69	2458412.892172 ± 0.000299	This Work
WASP-79 b	70	2458416.554571 ± 0.000311	This Work
WASP-79 b	73	2458427.541703 ± 0.000332	This Work
WASP-79 b	74	2458431.204093 ± 0.000347	This Work
WASP-79 b	75	2458434.866496 ± 0.000321	This Work
WASP-79 b	76	2458438.528882 ± 0.00029	This Work
WASP-79 b	77	2458442.191242 ± 0.000292	This Work
WASP-79 b	78	2458445.853639 ± 0.000326	This Work
WASP-79 b	79	2458449.515994 ± 0.000314	This Work
WASP-79 b	80	2458453.178366 ± 0.000317	This Work
WASP-79 b	81	2458456.840324 ± 0.000363	This Work
WASP-79 b	82	2458460.503155 ± 0.000335	This Work
WASP-62 b	−614	2455767.1533 ± 0.0005	Brown et al. (2017)
WASP-62 b	−140	2457858.41397 ± 0.000266	This Work*
WASP-62 b	−34	2458326.078168 ± 0.000293	This Work
WASP-62 b	−33	2458330.490547 ± 0.000294	This Work
WASP-62 b	−32	2458334.902385 ± 0.000315	This Work
WASP-62 b	−30	2458343.725961 ± 0.00025	This Work
WASP-62 b	−28	2458352.550282 ± 0.000278	This Work
WASP-62 b	−27	2458356.961811 ± 0.000257	This Work
WASP-62 b	−26	2458361.374157 ± 0.000268	This Work
WASP-62 b	−25	2458365.786076 ± 0.000295	This Work
WASP-62 b	−24	2458370.197678 ± 0.000244	This Work
WASP-62 b	−23	2458374.610308 ± 0.000284	This Work
WASP-62 b	−22	2458379.021593 ± 0.00025	This Work
WASP-62 b	−20	2458387.845506 ± 0.000238	This Work
WASP-62 b	−19	2458392.257448 ± 0.000258	This Work
WASP-62 b	−17	2458401.081679 ± 0.000286	This Work
WASP-62 b	−16	2458405.493547 ± 0.000294	This Work
WASP-62 b	−14	2458414.317213 ± 0.000241	This Work
WASP-62 b	−12	2458423.141634 ± 0.000372	This Work
WASP-62 b	−11	2458427.55355 ± 0.0003	This Work
WASP-62 b	−10	2458431.96504 ± 0.000233	This Work
WASP-62 b	−9	2458436.376957 ± 0.000258	This Work
WASP-62 b	−1	2458471.672875 ± 0.000281	This Work
WASP-62 b	−0	2458476.084548 ± 0.000273	This Work
WASP-62 b	1	2458480.496509 ± 0.000269	This Work
WASP-62 b	2	2458484.90846 ± 0.000263	This Work
WASP-62 b	3	2458489.320399 ± 0.000275	This Work
WASP-62 b	4	2458493.732346 ± 0.000274	This Work
WASP-62 b	5	2458498.144285 ± 0.000271	This Work
WASP-62 b	6	2458502.556272 ± 0.000263	This Work
WASP-62 b	7	2458506.968201 ± 0.000308	This Work
WASP-62 b	8	2458511.380161 ± 0.000259	This Work

*Data from HST

Table 7
Continuation of Table 6

Planet	Epoch	Midtime [BJD_{TDB}]	References
WASP-62 b	9	2458515.793014 ± 0.000308	This Work
WASP-62 b	10	2458520.203407 ± 0.00031	This Work
WASP-62 b	11	2458524.616007 ± 0.000263	This Work
WASP-62 b	14	2458537.851688 ± 0.000269	This Work
WASP-62 b	16	2458546.675279 ± 0.000324	This Work
WASP-62 b	17	2458551.087738 ± 0.000337	This Work
WASP-62 b	19	2458559.91167 ± 0.000278	This Work
WASP-62 b	20	2458564.323603 ± 0.000285	This Work
WASP-62 b	22	2458573.147116 ± 0.000311	This Work
WASP-62 b	23	2458577.559142 ± 0.000317	This Work
WASP-62 b	25	2458586.382966 ± 0.000333	This Work
WASP-62 b	26	2458590.795328 ± 0.000345	This Work
WASP-62 b	27	2458595.206831 ± 0.000331	This Work
WASP-62 b	29	2458604.031175 ± 0.00029	This Work
WASP-62 b	30	2458608.443135 ± 0.000301	This Work
WASP-62 b	31	2458612.855056 ± 0.000311	This Work
WASP-62 b	32	2458617.266322 ± 0.000359	This Work
WASP-62 b	33	2458621.67842 ± 0.000344	This Work
WASP-62 b	34	2458626.090956 ± 0.000358	This Work
WASP-62 b	35	2458630.502921 ± 0.000265	This Work
WASP-62 b	36	2458634.914867 ± 0.000257	This Work
WASP-62 b	38	2458643.738117 ± 0.000318	This Work
WASP-62 b	39	2458648.150206 ± 0.000305	This Work
WASP-62 b	40	2458652.561559 ± 0.000312	This Work
WASP-62 b	41	2458656.974299 ± 0.000292	This Work
WASP-62 b	42	2458661.385862 ± 0.000292	This Work
WASP-62 b	43	2458665.798175 ± 0.000285	This Work
WASP-62 b	44	2458670.210186 ± 0.000304	This Work
WASP-62 b	45	2458674.621865 ± 0.000315	This Work
WASP-62 b	46	2458679.034395 ± 0.000284	This Work

Note. All midtimes reported in this work are from TESS unless otherwise stated.

ORCID iDs

Nour Skaf https://orcid.org/0000-0002-9372-5056
Billy Edwards https://orcid.org/0000-0002-5494-3237
Quentin Changeat https://orcid.org/0000-0001-6516-4493
Mario Morvan https://orcid.org/0000-0001-8587-2112
Tiziano Zingales https://orcid.org/0000-0001-6880-5356
Ahmed Al-Refaie https://orcid.org/0000-0003-2241-5330
Benjamin Charnay https://orcid.org/0000-0003-0977-6545
Angelos Tsiaras https://orcid.org/0000-0003-3840-1793
Olivia Venot https://orcid.org/0000-0003-2854-765X
Ingo Waldmann https://orcid.org/0000-0002-4205-5267
Jean-Philippe Beaulieu https://orcid.org/0000-0003-0014-3354

References

Abel, M., Frommhold, L., Li, X., & Hunt, K. L. 2011, JPCA, 115, 6805
Abel, M., Frommhold, L., Li, X., & Hunt, K. L. 2012, JChPh, 136, 044319
Addison, B. C., Tinney, C. G., Wright, D. J., et al. 2013, ApJL, 774, L9

Al-Refaie, A. F., Changeat, Q., Waldmann, I. P., & Tinetti, G. 2019, arXiv:1912.07759
Astropy Collaboration, Price-Whelan, A. M., Sipőcz, B. M., et al. 2018, AJ, 156, 123
Batalha, N. M., Rowe, J. F., Bryson, S. T., et al. 2013, ApJS, 204, 24
Batygin, K., & Stevenson, D. J. 2010, ApJL, 714, L238
Batygin, K., Stevenson, D. J., & Bodenheimer, P. H. 2011, ApJ, 738, 1
Baudino, J.-L., Bézard, B., Boccaletti, A., et al. 2015, A&A, 582, A83
Bean, J. L., Stevenson, K. B., Batalha, N. M., et al. 2018, PASP, 130, 114402
Benneke, B., & Seager, S. 2012, ApJ, 753, 100
Bonomo, A. S., Desidera, S., Benatti, S., et al. 2017, A&A, 602, A107
Bourrier, V., des Etangs, A. L., & Vidal-Madjar, A. 2015, A&A, 573, A11
Brandl, B. R., Absil, O., Agócs, T., et al. 2018, Proc. SPIE, 10702, 107021U
Brogi, M., Snellen, I. A. G., de Kok, R. J., et al. 2012, Natur, 486, 502
Brown, D. J. A., Triaud, A. H. M. J., Doyle, A. P., et al. 2017, MNRAS, 464, 810
Burgasser, A. J., Marley, M. S., Ackerman, A. S., et al. 2002, ApJL, 571, L151
Caldas, A., Leconte, J., Selsis, F., et al. 2019, A&A, 623, A161
Cassan, A., Kubas, D., Beaulieu, J.-P., et al. 2012, Natur, 481, 167
Changeat, Q., Edwards, B., Waldmann, I. P., & Tinetti, G. 2019, ApJ, 886, 39
Charnay, B., Bézard, B., Baudino, J.-L., et al. 2018, ApJ, 854, 172
Chen, G., Pallé, E., Welbanks, L., et al. 2018, A&A, 616, A145
Claret, A. 2000, A&A, 363, 1081
Collette, A. 2013, Python and HDF5 (Sebastopol, CA: O'Reilly & Associates)
Cushing, M. C., Marley, M. S., Saumon, D., et al. 2008, ApJ, 678, 1372
Dressing, C. D., & Charbonneau, D. 2013, ApJ, 767, 95
Dulick, M., Bauschlicher, C. W., Jr., Burrows, A., et al. 2003, ApJ, 594, 651
Eastman, J., Siverd, R., & Gaudi, B. S. 2010, PASP, 122, 935
Edwards, B., Changeat, Q., Baeyens, R., et al. 2020a, AJ, 160, 8
Edwards, B., Changeat, Q., Yip, K. H., et al. 2020b, MNRAS, in press
Edwards, B., Mugnai, L., Tinetti, G., Pascale, E., & Sarkar, S. 2019, AJ, 157, 242
Edwards, B., Rice, M., Zingales, T., et al. 2018, ExA, 47, 29
Ehrenreich, D., Lovis, C., Allart, R., et al. 2020, Natur, 580, 597
Fanson, J., McCarthy, P. J., Bernstein, R., et al. 2018, Proc. SPIE, 10700, 1070012
Feroz, F., Hobson, M. P., & Bridges, M. 2009, MNRAS, 398, 1601
Fletcher, L. N., Gustafsson, M., & Orton, G. S. 2018, ApJS, 235, 24
Foreman-Mackey, D., Hogg, D. W., Lang, D., & Goodman, J. 2013, PASP, 125, 306
Fortney, J. J., Lodders, K., Marley, M. S., & Freedman, R. S. 2008, ApJ, 678, 1419
Fu, G., Deming, D., Knutson, H., et al. 2017, ApJL, 847, L22
Greene, T. P., Line, M. R., Montero, C., et al. 2016, ApJ, 817, 17
Griffith, C. A. 2014, RSPTA, 372, 20130086
Heng, K., & Kitzmann, D. 2017, MNRAS, 470, 2972
Heng, K., Menou, K., & Phillipps, P. J. 2011, MNRAS, 413, 2380
Hoeijmakers, H. J., Ehrenreich, D., Heng, K., et al. 2018, Natur, 560, 453
Howard, A. W. 2013, Sci, 340, 572
Hubeny, I., Burrows, A., & Sudarsky, D. 2003, ApJ, 594, 1011
Hunter, J. D. 2007, CSE, 9, 90
Kass, R. E., & Raftery, A. E. 1995, J. Am. Stat. Assoc., 90, 773
Lam, K. W. F., Faedi, F., Brown, D. J. A., et al. 2017, A&A, 599, A3
Leconte, J., Chabrier, G., Baraffe, I., & Levrard, B. 2010, A&A, 516, A64
Li, G., Gordon, I. E., Rothman, L. S., et al. 2015, ApJS, 216, 15
Lithwick, Y., & Wu, Y. 2014, PNAS, 111, 12610
Lodders, K. 2002, ApJ, 577, 974
Lodders, K. 2019, arXiv:1912.00844
MacDonald, R. J., Goyal, J. M., & Lewis, N. K. 2020, ApJL, 893, L43
Madhusudhan, N. 2012, ApJ, 758, 36
Madhusudhan, N., Agúndez, M., Moses, J. I., & Hu, Y. 2016, SSRv, 205, 285
Majeau, C., Agol, E., & Cowan, N. B. 2012, ApJL, 747, L20
Mazeh, T., Holczer, T., & Faigler, S. 2016, A&A, 589, A75
McKinney, W. 2011, pandas: A Foundational Python Library for Data Analysis and Statistics, https://www.dlr.de/sc/portaldata/15/resources/dokumente/pyhpc2011/submissions/pyhpc2011_submission_9.pdf
Morello, G., Claret, A., Martin-Lagarde, M., et al. 2020, AJ, 159, 75
Mugnai, L. V., Pascale, E., Edwards, B., Papageorgiou, A., & Sarkar, S. 2020, ExA, submitted
Oliphant, T. E. 2006, A Guide to NumPy, Vol. 1 (Spanish Fork, UT: Trelgol Publishing)
Owen, J. E., & Lai, D. 2018, MNRAS, 479, 5012
Palle, E., Chen, G., Prieto-Arranz, J., et al. 2017, A&A, 602, L15
Pinhas, A., Madhusudhan, N., Gandhi, S., & MacDonald, R. 2018, MNRAS, 482, 1485
Pinhas, A., Madhusudhan, N., Gandhi, S., & MacDonald, R. 2019, MNRAS, 482, 1485
Pluriel, W., Zingales, T., Leconte, J., & Parmentier, V. 2020, A&A, 636, A66
Polyansky, O. L., Kyuberis, A. A., Zobov, N. F., et al. 2018, MNRAS, 480, 2597
Rauscher, E., & Menou, K. 2013, ApJ, 764, 103
Ricker, G. R., Winn, J. N., Vanderspek, R., et al. 2014, Proc. SPIE, 9143, 914320
Rocchetto, M., Waldmann, I. P., Venot, O., Lagage, P. O., & Tinetti, G. 2016, ApJ, 833, 120
Rodler, F. 2018, in Handbook of Exoplanets, ed. H. Deeg & J. Belmonte (Cham: Springer), 194
Rothman, L. S., Gamache, R. R., Goldman, A., et al. 1987, ApOpt, 26, 4058
Rothman, L. S., Gordon, I. E., Barber, R. J., et al. 2010, JQSRT, 111, 2139
Sharp, C. M., & Burrows, A. 2007, ApJS, 168, 140
Showman, A. P., Fortney, J. J., Lian, Y., et al. 2009, ApJ, 699, 564
Sing, D. K., Fortney, J. J., Nikolov, N., et al. 2016, Natur, 529, 59
Sing, D. K., Fortney, J. J., Nikolov, N., et al. 2016, Natur, 529, 59
Skidmore, W., Anupama, G. C., & Srianand, R. 2018, arXiv:1806.02481
Sotzen, K. S., Stevenson, K. B., Sing, D. K., et al. 2020, AJ, 159, 5
Spake, J. J., Sing, D. K., Wakeford, H. R., et al. 2020, MNRAS, submitted
Stevenson, K. B., Désert, J.-M., Line, M. R., et al. 2014, Sci, 346, 838
Swain, M. R., Vasisht, G., & Tinetti, G. 2008, arXiv:0802.1030
Tennyson, J., & Yurchenko, S. 2018, Atoms, 6, 26
Tennyson, J., Yurchenko, S. N., Al-Refaie, A. F., et al. 2016, JMoSp, 327, 73
Tinetti, G., Drossart, P., Eccleston, P., et al. 2018, ExA, 46, 135
Tinetti, G., Vidal-Madjar, A., Liang, M.-C., et al. 2007, Natur, 448, 169
Tsiaras, A., Rocchetto, M., Waldmann, I. P., et al. 2016a, ApJ, 820, 99
Tsiaras, A., Waldmann, I., Rocchetto, M., et al. 2016c, pylightcurve: Exoplanet lightcurve model, Astrophysics Source Code Library, ascl:1612.018
Tsiaras, A., Waldmann, I. P., Rocchetto, M., et al. 2016b, ApJ, 832, 202
Tsiaras, A., Waldmann, I. P., Tinetti, G., Tennyson, J., & Yurchenko, S. N. 2019, NatAs, 3, 1086
Tsiaras, A., Waldmann, I. P., Zingales, T., et al. 2018, AJ, 155, 156
Virtanen, P., Gommers, R., Oliphant, T. E., et al. 2020, NatMe, 17, 261
Visscher, C., Lodders, K., & Fegley, B. 2010, ApJ, 716, 1060
Waldmann, I. P., Rocchetto, M., Tinetti, G., et al. 2015a, ApJ, 813, 13
Waldmann, I. P., Tinetti, G., Rocchetto, M., et al. 2015b, ApJ, 802, 107
Woitke, P., Helling, C., Hunter, G. H., et al. 2018, A&A, 614, A1
Wright, J. T., Marcy, G. W., Howard, A. W., et al. 2012, ApJ, 753, 160
Yip, K. H., Waldmann, I. P., Tsiaras, A., & Tinetti, G. 2019, arXiv:1811.04686
Yurchenko, S. N., Barber, R. J., & Tennyson, J. 2011, MNRAS, 413, 1828
Yurchenko, S. N., & Tennyson, J. 2014, MNRAS, 440, 1649